The transition from granite to banded aplite-pegmatite sheet complexes: an example from Megiliggar Rocks, Tregonning topaz granite, Cornwall

K. Breiter, J. Ďurišová, T. Hrstka, Z. Korbelová, Institute of Geology of the Czech Academy of Sciences, Rozvojová 269, CZ-16500 Praha, Czech Republic

M. Vašinová Galiová, Department of Chemistry, Faculty of Science, Masaryk University, Kotlářská 2, CZ-611 37 Brno, Czech Republic; actual address: Department of Geology and Pedology, Faculty of Forestry and Wood Technology, Mendel University in Brno, Zemědělská 1, 613 00 Brno, Czech Republic

A. Müller, Natural History Museum, University of Oslo, P.O.Box 1172, Blindern, 0318 Oslo, Norway; Natural History Museum, Cromwell Road, London SW7 5BD, United Kingdom

B. Simons, 14 Park an Fenten, St. Agnes, Cornwall, TR5 0A5, United Kingdom

R.K. Shail, B.J. Williamson, J.A. Davies, Camborne School of Mines, College of Engineering, Mathematics and Physical Sciences, University of Exeter, Penryn Campus, Cornwall, TR10 9FE, United Kingdom

Abstract

The genetic relationship between a granite pluton and adjacent complex of rare-metal pegmatite-aplite-banded sheets (Megiliggar Sheet Complex - MSC) has been studied at the border of the Tregonning topaz granite at Megiliggar Rocks, Cornwall, SW England. Similarities in whole-rock chemical and mineralogical compositions, together with a gradual change in textures away from the granite margin, provide strong evidence for a genetic link between the Tregonning Granite and MSC. The sheets are likely to represent apophyses of residual melt which escaped from the largely crystallised roof of the granite pluton. The escaping melt was peraluminous, had a composition near the F, B, Li slightly enriched granite minimum, and, in comparison with other Cornish granites, was enriched in F, Li, Rb, Cs, Sn, W, Nb, Ta, and U, and depleted in Fe, Mg, Ca, Sr, Th, Zr, and REE. With increasing distance from the Tregonning Granite, the silicate melt crystallized as homogeneous

leucogranite sheets and banded complex sheets (i.e. combinations of bands with granitic, aplitic and pegmatitic textures), then layered aplite-pegmatites; this sequence becoming progressively more depleted in the fluxing and volatile elements F, Li, Rb, and Cs, but showing no change in Zr/Hf ratios. The fixed Zr/Hf ratio is interpreted as indicating a direct genetic link (parental melt) between all rock types, however the melt progressively lost fluxing and volatile elements with distance from the granite pluton, probably due to wall-rock reaction or fluid exsolution and migration via fractures. Differentiation of the primary melt into Na-Li-F-rich and separate K-B-rich domains was the dominant chemical process responsible for the textural and mineral diversity of the MSC. On a large (cliff-section) scale, the proximal Na-Li-F-rich leucogranite passes through complex sheets into K-B-rich aplite-pegmatites, whilst at a smaller (< 1 m) scale, the K-B-rich bands are interspersed (largely overlain) by Na-Li-F-rich segregations. The grain size differences between the aplite and pegmatite could be related to pressure fluctuations and/or undercooling.

Key words: granite; aplite; pegmatite; magmatic layering; Megiliggar Rocks; Cornwall

1. Introduction

The genetic relationship between granitic pegmatites and adjacent or enclosing granites has long been debated, particularly whether such pegmatites form from residual, volatile-rich melts sourced from the granites (London, 2008, chapter 5). In the case of pericontact pegmatites, e.g. stockscheider in tin granites in the Erzgebirge (Breiter et al., 2005), and intragranitic pegmatites, e.g. Black Hills, South Dakota (Norton, 1994) or Pikes Peak, Colorado (Simmons and Heinrich, 1975), a direct genetic link is generally accepted. Stockscheider represent an early product of volatile enrichment at the upper or lateral contacts of a granite melt with non-granite host rocks or a previously emplaced melt batch (Breiter et al., 2005). Intragranitic pegmatites represent late segregations of residual water-rich melt (Shearer et al., 1992). These pegmatite types are commonly found in both strongly peraluminous and subaluminous (S- and A-type) granite plutons.

In the case of typical “classic pegmatites”, i.e. large dykes or bodies with strong internal zoning and enrichment of rare minerals/elements, typically intruded into metamorphic rocks distal from granite

plutons of appropriate composition, the source of the pegmatitic melt is often inferred (London 2008, chapter 10). Goad and Černý (1981) introduced the term "fertile granite" for the mainly leucocratic granitic plutons which lie proximal to pegmatite fields (mainly of LCT-type). These fulfil the theoretical expectations for fertile starting compositions coupled with long fractionation processes, forming bodies of complex pegmatites (Černý, 1991; Breaks and Moore, 1992). Nevertheless, despite an intensive search, localities enabling the direct study of the transition from a granite pluton to rare-element pegmatite dykes in the host rock are scarce (Neiva and Ramos, 2010; Autunes et al., 2013). We describe here a superb example from Megiliggar Rocks in Cornwall, SW England. A subhorizontal sheet complex, showing the transition from leucogranites to aplites and pegmatites, is spectacularly displayed over 500 m of coastal cliff exposures at the SE margin of the Tregonning Granite. Although the locality is well-known, published mineralogical investigations and data are relatively sparse (Hall, 1930; Hosking, 1952; Stone, 1969, 1975, 1992; Stone and George, 1978; Badham, 1980; George et al., 1981; Exley and Stone, 1982; Stone et al., 1988; Henderson et al., 1989; Bromley, 1989; Floyd et al., 1993; Breiter et al., 2016; Duchoslav et al., 2017; Simons et al., 2017); the most comprehensive study of aplite-pegmatite banding is that of Stone (1969). The aims of this study are to describe the mineralogy, mineral chemistry and whole-rock geochemistry of the entire range of granitic rocks within the Megiliggar sheets (granites, aplites, pegmatites) and ascertain their relationship(s) with each other and the adjacent Tregonning Granite.

2. Geological setting

The Early Permian Cornubian Batholith of SW England is a classic location for the study of rare-metal granites (e.g. Manning and Exley, 1984; Stone and Exley, 1985; Charoy, 1986; Willis-Richards and Jackson, 1989; Chappell and Hine, 2006; Müller et al., 2006; Simons et al., 2016). These Variscan post-collisional peraluminous granites can be subdivided into five major types (Fig. 1a): two mica (G1), muscovite (G2), biotite (G3), tourmaline (G4) and topaz (G5) granites. The topaz granites are typically medium-grained, equigranular and aphyric alkali feldspar granites ($<An_5$), and are characterized by lithium-rich micas and up to 3 vol.% topaz (Manning and Hill, 1990; Manning et al., 1996; Stone, 1992; Simons et al., 2016). Topaz granites occur principally in the Tregonning Granite

and the Nanpean and Hensbarrow stocks within the composite St Austell Granite; the Meldon Dyke, north of the Dartmoor Granite, is a topaz aplite (Simons et al., 2016).

The Tregonning-Godolphin Granite (Stone, 1975, 1992) contains the fine- to medium-grained porphyritic two mica Godolphin Granite in the north, and the Tregonning Granite in the central and southern parts of the pluton which is exposed on the coast. Hall (1930) attributed these coastal exposures to the Godolphin Granite, following early Geological Survey usage (Reid and Flett, 1907), but the composite nature of the pluton was recognised by Stone (1960) and the Tregonning Granite has been distinguished separately in most subsequent work (e.g. Stone, 1975, 1990; Floyd et al., 1993; Simmons et al., 2016).

The host rocks to the Tregonning Granite are low-grade regionally- and contact-metamorphosed metasedimentary rocks of the Mylor Slate Formation (Goode and Taylor, 1988; Leveridge and Shail, 2011). Field relations indicate that granite emplacement and contact-metamorphism post-dated the development of folds and cleavages related to both Variscan thrusting (D1 and D2) and post-Variscan extension (D3) (Stone, 1966, 1975; Alexander and Shail, 1996; Pownall et al., 2012). The dominant fabric in the host rocks is a gently SE-dipping S3 crenulation cleavage (S2 of Stone, 1966) that commonly transposes earlier fabrics and locally contains variably boudinaged veins of metamorphic quartz (Alexander and Shail, 1996). The history of pre- and post-granite vein development and the associated fluid characteristics has been described by Wilkinson (1990, 1991) and Gleeson et al. (2000).

A series of leucocratic, partly layered granites, termed the "roof complex" (Stone, 1975), lies along the horizontal upper contact of the Tregonning Granite with the Mylor Slate Formation. At the SE margin of the Tregonning Granite, the roof complex is represented by gently SE-dipping leucogranite and aplite-pegmatite sheets within the Mylor Slate Formation that are continuously exposed in a 30-50 m high cliff section over a distance of *c.* 500 m between Legereath Zawn ("zawn" is a Cornish term meaning a deep and narrow sea-inlet cut by erosion into sea-cliffs, and with steep or vertical side-walls) and Tremearne Par ("Megiliggar Rocks" 50°04´26.4´´ N, 5°24´42.6´´ W) (Fig. 2a). We hereafter refer collectively to these sheets as the "Megiliggar Sheet Complex" (MSC). The geometrical

relations of these sheets, and their relations to the Tregonning Granite, have been variably represented in sketch cross-sections (Hall, 1930; Stone, 1975; Badham, 1980; Exley and Stone, 1982; Bromley, 1989; Floyed et al., 1993; Fig. 1b in this work).

The easternmost exposure of the Tregonning Granite occurs around Legereath Zawn where it post-dates an earlier biotite granite porphyry ('elvan') dyke (Hall, 1930), the 'Legereath granite porphyry' of Stone (1975) or 'Legereath Zawn Elvan' of Breiter et al. (2016). The uppermost part of the Tregonning Granite is exposed in the western, northern and eastern walls of Legereath Zawn. In the northern wall it occupies the full cliff height (50 m) but moving eastwards passes, at an elevation of *c.* 15 m, into the lowermost sheet of the MSC within the Mylor Slate Formation. We concur with Hall (1930, Fig. 8B) that there is also a magmatic linkage, via a short sheet segment, between this lowermost sheet and the uppermost part of the Tregonning Granite towards the base of the cliff on the eastern side of Legereath Zawn. Although the contacts between the more easterly MSC sheets and the Tregonning Granite are not exposed, we infer that all the MSC was sourced in a comparable manner from the upper parts of the Tregonning Granite.

3. Analytical methods

The whole-rock (WR) major element oxide determinations (using wet techniques, for detail see http://www.geology.cz/extranet-eng/services/laboratories/inorganic-analysis) were carried out at the Czech Geological Survey, Praha. Replicate analyses of an international reference material (JG-3; Geological Survey of Japan) yielded an average error (1 sigma) of ± 1 % with respect to the recommended values (Govindaraju, 1994). Trace elements were determined by ICP mass spectrometry following lithium metaborate/tetraborate fusion or nitric acid digestion in the laboratories of the Bureau Veritas, Vancouver, Canada (For details including limits of detection see http:// http://acmelab.com/wp-content/uploads/2009/03/BVM_2017-Fee-Schedule_v4_14Sep2017.pdf, laboratory codes LF100 and MA200).

A TESCAN Integrated Mineral Analyzer (TIMA) was used for automated mineralogical, modal and textural analysis employing Liberation Analysis mode (Gottlieb et al., 2000). Liberation Analysis mode, with 'high-resolution mapping', includes the collection of backscattered electron (BSE) and

EDS data on a regular grid (10 μm point spacing in our case). At each point, the BSE level is determined. If the BSE level is above a certain threshold, the beam is kept directed on this spot until a predefined number of X-ray counts (1000 in our case) from the spectrometer are collected. The individual points are grouped based on a similarity search algorithm and areas of coherent BSE and EDS data merged to produce segments (i.e. mineral grains). Individual spectra from points within each segment are summed. The average BSE value is also calculated. Data from each segment are then compared against a classification scheme to identify the mineral and assign its chemistry and density (Hrstka et al., in prep.). The results are plotted in the form of a map showing the distribution of minerals within the sample.

Minerals were chemically analysed using a Cameca SX 100 electron microprobe, in wavelength-dispersive mode, at the Institute of Geology CAS. Analytical conditions for silicates were: accelerating voltage 15 kV, beam current 10 nA, beam diameter 2 μm. The following calibration standards were used: Na, Al – jadeite, Mg, Si, Ca – diopside, K – leucite, Ti – rutile, P – apatite, Mn – $MnCr_2O_4$, Fe – magnetite, F – fluorite, and Rb – RbCl. The matrix correction procedure X-Phi (Merlet, 1994) was applied. The empirical formulae of the feldspars were calculated based on 8 oxygen atoms per formula unit (8 O apfu); the empirical formulae of the micas were calculated based on 44 negative charges. The empirical formulae of the tourmaline were calculated based on 24.5 oxygen atoms per formula unit (boron excluded).

The Sn, W, Nb, Ta-oxide minerals and zircon were analyzed at an accelerating voltage and beam current of 15 kV and 7 nA, and 15 kV and 10 nA, respectively, with a beam diameter of 1 to 3 μm. The counting times on each peak were optimized for individual elements according to their expected concentrations (10–60 s), and half that time was used to obtain background counts. X-ray lines and background offsets were selected to minimize interference.

Lithium and trace elements in micas and tourmalines were determined using LA-ICP-MS at the Masaryk University, Brno. Micas were analyzed using a Nd:YAG-based laser ablation system at a wavelength of 213 nm (New Wave Research, Inc., Fremont, CA, USA), which was coupled to a ICP-QMS instrument with quadrupole mass spectrometer (Agilent 7500ce, Agilent Technologies, Santa Clara, CA, USA). Tourmaline grains were analyzed with an ArF* excimer-based laser ablation system

Analyte G2 (Teledyne CETAC Technologies) at a wavelength of 193 nm, which was coupled to an Element2 (Thermo Fischer Scientific) ICP-MS instrument with double focusing electrostatic and magnetic sectors. Operating conditions of both the LA-ICP-QMS and LA-ICP-SFMS were optimized with the aim of obtaining maximum signal-to-background ratios and sensitivity, minimum spectral and non-spectral interferences and best signal stability, and then kept constant throughout the analyses. Micas were ablated under optimal conditions of: fluence (13 $J \cdot cm^{-2}$), frequency (10 Hz), ablation dwell time (40 s), duration of Ar-He gas blank measurement (40 s) and laser beam spot diameter (80 μm). For tourmaline, a spot diameter of 30 μm, fluence of 3 $J \cdot cm^{-2}$, frequency of 10 Hz, 60s ablation dwell time and 60s Ar-He gas blank measurement were applied. Silica was employed as the internal reference element having been previously determined in samples by electron microprobe. The systems were calibrated using artificial glass NIST610 and NIST612 to quantify the concentrations of Li, Al, Sc, Ga, Ge, Nb, In, Sn, Cs, Ta, W and Tl in mica, and Li, Be, B, Al, Sc, Zn, Ga, Ge, Rb, Nb, In, Sn, Cs, W, and Tl in tourmaline.

Trace element concentrations (Al, B, Be, Fe, Ge, Li, Mn, P, Rb, Sn, Sr, and Ti) in quartz were determined by LA-ICP-MS at the Institute of Geology CAS. This utilized a Thermo-Finnigan Element 2 sector field mass spectrometer coupled to an Analyte Excite 193 nm excimer laser (Photon Machines). Analyses were conducted using a repetition rate of 10-20 Hz, laser fluence of 3–5 J/cm^2, beam size of 40-80 μm; all parameters were optimized against the intensity of signals. The ablated material was transported by high purity He gas from the laser ablation cell. Time-resolved signal data were processed using Glitter software (http://www.glitter-gemoc.com/). The isotopes ^{29}Si and ^{30}Si were used as internal standards based on the assumption that the analyzed quartz contains 99.95 wt% SiO_2. The data were calibrated using artificial glass NIST612. For more details see Breiter et al. (2013).

4. Petrology of the Megiliggar Sheet Complex (MSC)

4.1 Textural varieties of MSC samples studied

The Tregonning Granite is a medium-grained equigranular granite, light in colour and composed of quartz, albite, perthitic K-feldspar, zinnwaldite/lepidolite micas, and Li-F-rich schorl. Apatite is minor, while rutile, Fe-columbite, and zircon are accessory (typical sample **#5303,** Fig. 3a).

A small body of fine-grained equigranular granite with macroscopic black mica, termed a biotite granite dyke, was found within the faulted zone at Legereath Zawn, in association with a typical granite-porphyry ('elvan') dyke. The biotite granite is composed of quartz, albite, K-feldspar, strongly muscovitized Li-Fe-mica (primarily siderophyllite–zinnwaldite in composition) and schorl. Apatite is minor; rutile, zircon and monazite are accessory minerals (sample **#4962**).

SE from Legereath Zawn, the following principal types (facies) can be defined within the sheets of the MSC (Fig. 1b):

- Homogeneous leucogranite which forms three major sheets, each up to 3 m thick and 200 m long (Fig. 2a). This rock is fine- to medium grained, equigranular and nearly white in colour. It is composed of quartz, albite>K-feldspar, zinnwaldite-trilithionite mica, and Li-enriched fluoro-schorl. Sub-parallel dark layers up to 3 cm thick that are enriched in mica are locally conspicuous (Fig. 2b, c). Amblygonite and apatite are minor; zircon, Mn-columbite, and uraninite are accessory (typical sample #**4963**).
- These fine-to medium grained leucogranite sheets also contain a fine-layered aplitic facies and minor pods and laminae of pegmatite facies. Further SE, the proportions of granitic, aplitic and pegmatitic facies became nearly equal forming "complex sheets" (Fig. 2d, e). Some aplitic and pegmatitic layers form rhythmic structures; textural borders are smooth and gradational. The direction of crystallization, i.e. relative age of layers, may be inferred from orientation of feldspar crystals in unidirectional solidification textures (UST) (London, 2008). In some cases, the layering is a product of repeated injection (compare Bromley, 1989) with symmetrical zoning. These sheets are enriched in Li and F; they contain pinkish Li-bearing zinnwaldite–trilithionite micas and Li-enriched (deep green) tourmaline in some laminae, but muscovite and black schorl in others. Albite dominates over K-feldspar. Manganese-rich apatite is minor; fluorite, monazite, xenotime, zircon, columbite, rutile, cassiterite, wolframite, uraninite, pyrite, arsenopyrite, molybdenite and native Bi are accessory minerals. Typical samples are **#2015** (fine layered aplite), **4964** (fine-

grained granite with pegmatitic laminae), **5304** (fine-grained granite rich in tourmaline), **5305** (layered combination of granite, pegmatite and aplite, Fig. 3b).

- Major bodies of aplite/coarse-grained granite/pegmatite and abundant thinner aplite/pegmatite sheets with very different textures and scales of layering appear mainly in flat outcrops on the beach, and are subordinate in the cliff. They are composed of irregular and locally interpenetrative domains (layers, nests, dykes) of <1 mm-sized (aplitic), 1–2 cm-sized (granitic) and coarser (pegmatitic) matter. Contacts are both sharp and gradational; in-situ fractionation is combined here with repeated injection of similar magma (thin laminas crystallizing from both contacts inwards cross an older layering with upwards oriented crystallization). All textural varieties within these sheets contain more K-feldspar than albite, and are rich in tourmaline (schorl to foitite). Mica is in all cases muscovite/phengite in composition. Apatite is minor, and zircon, monazite, xenotime, uraninite, sphalerite, pyrite, molybdenite, and native Bi are accessory. Rocks are Li- and F-poor. Typical samples are #**4965** (layered aplite from centre of a thick sheet), #**5306** (aplite at the border of a sheet), and #**5307** (granitopegmatite, i.e. very coarse grained rock with granitic texture, centre of the sheet next to #5306, Fig. 3c). Quartz-cored tourmaline is also present (very coarse-grained granite, #**5302**).
- Thin pegmatite or aplite/pegmatite dykes (usually <20 cm, Figs. 3b, c) occur in the eastern part of the cliff. These dykes often change orientation (horizontal vs. vertical), diverge and coalesce. The pegmatite-like textures appear mainly along the contacts (Fig. 3d), but locally change laterally to pericontact and central positions (Fig. 2f). These dykes are tourmaline and muscovite-dominant, and Li- and F-poor. Occasionally, texturally similar, but steeply-inclined sheets occur (Fig. 2g).
- Quartz veins, variably developed throughout the study area, but conspicuous in the easternmost part around Tremearne Par (Hosking, 1952; Badham, 1980; Bromley, 1989). These are deformed (folded and/or boudinaged) within the S3 cleavage and pre-date granite emplacement; they were sourced from Variscan metamorphic fluids and are not part of the MSC.

For further description and interpretation, samples have been classified into three principal groups, based on a combination of textures, whole-rock chemistry, and mineral abundances and compositions:

(i) **granites**, i.e. fine- to medium-grained homogeneous rocks (Tregonning Granite #5303, leucogranite sheet #4963), (ii) Li-mica-dominated **complex sheets** (#2015, 4964, 5305, 5304), and (iii) muscovite-tourmaline-dominated **aplite-pegmatites** (#4965, 5302, 5306, 5307) [The term aplite-pegmatite is hereafter used for intimate banding of fine-grained (aplitic) and coarse-grained (pegmatitic) layers (Jahns and Tuttle, 1963; London, 2008)] . This classification is somewhat simplistic, as combinations of textural types and transitional facies are common, but is necessary to allow further description, interpretation, and discussion.

4.2 Detail zoning of the sheets

Two samples of fine-layered rock were chosen for a detailed study of mineralogical and geochemical zoning: a Li-mica dominated sample from a complex sheet (#2015, Fig. 4), and a muscovite-tourmaline-dominated aplitic domain of an aplite-pegmatite sheet (#4965, Fig. 5). Mineral maps across the zoning were constructed and mineral compositions in texturally distinct layers (laminae) were computed using TIMA-technology. Approximate chemical compositions of individual layers and WR (Fig. 6, Supplementary tables 1, 2) were computed from modal compositions of layers and chemical composition of rock-forming minerals determined by electron microprobe, with Li by the LA-ICP-MS.

The texture of sample #2015, from a Li, F-enriched complex sheet, is composite and can be divided into three sections. The lower part of the sequence, termed layers #1→7, evolved systematically with a decrease in the modal abundance of K-feldspar (28→6.5 vol.%), quartz (33→25 vol.%), and tourmaline (8→4 vol.%), along with a strong increase in the modal abundance of albite (16→74 vol.%, Fig. 4). In the middle section, lines 8→11, the modal abundance of minerals is much more variable, as it is in the upper part of the sample, layers #12→22, which is also rich in albite (38–74 vol.%), zinnwaldite (mostly 5–6 vol.%) and topaz (up to 11 vol.% in lines 19 and 20), and poor in K-feldspar (mostly <10 vol.%), tourmaline (mostly <1 vol.%) and muscovite (mostly <2 vol.%). Additionally, the grain size of the albite-dominated layers is significantly finer than that of K-feldspar dominated layers.

Distinctive chemical changes appear between layers #11 and 12: K and B decrease, while F increases (Fig. 6a). Mineralogically, this is due to muscovite and tourmaline giving way to zinnwaldite and topaz. The pairs Na–K and F–B are negatively correlated (Fig. 6b, c) due to mineralogical antagonism of albite vs. K.-feldspar and lepidolite vs. tourmaline. Boron and Fe show a positive trend (Fig. 6d), both hosted dominantly in tourmaline, and F with Mn, as F-rich micas are relatively enriched in Mn. The relationship between F and B vs. the Ab-Kfs ratio is more complex; nevertheless, F- (resp. B-) enrichment in Ab- (resp. Kfs-) dominated layers is clear.

The tourmaline-muscovite aplite-pegmatite is dominated by aplite (#4965, Fig. 5) and shows only moderate variability in mineral compositions in layers #1-5, with 23–42 vol.% K-feldspar, 12–26 vol.% albite, 30–47 vol.% quartz, 4–8 vol.% muscovite and 4–10 vol.% schorl. The zoning is visually apparent from a variation in grainsize and orientation of tourmaline grains. There is no general trend in composition from layers #1→5. Layer #6 differs remarkably and is rich in topaz and muscovite (22.4 and 32.4 vol.% resp.), representing a vug filled with residual melt/fluid. Surprisingly, even though sample #4965 contains F-poor tourmaline and mica, the WR content of fluorine is, due to the high topaz vol.% in layer #6, higher than that in sample #2015 (Fig. 6c).

5. Whole-rock chemical compositions

All rock types forming the MSC are chemically similar, being rich in silica (69–76 wt.% SiO_2), leucocratic, and strongly peraluminous (ASI=1.23–1.46, (molar $Al_2O_3/CaO+K_2O+Na_2O$)) (Tab.1, Fig. 7). All rock types are, in comparison with other Cornubian granites, rich in alumina (mostly 14–16 wt.% Al_2O_3), phosphorus (0.3–0.7 wt.% P_2O_5), Li, Nb, Ta and Sn, but poor in iron (mostly <1 wt.% FeO_{tot}), magnesium (mostly <0.2 wt.% MgO), calcium (with one exception ≤0.6 wt.% CaO), Zr and REE (Chappell and Hine, 2006; Simons et al., 2016).

Comparing the three main groups of rocks, the granites (comprising the Tregonning Granite and leucogranite sheet) are relatively poor in silica (69.2–71.1 wt.% SiO_2) and potassium (4.2–5.3 wt.% K_2O), but rich in sodium (3.4–4.3 wt.% Na_2O), lithium (ca. 0.40 wt.% Li_2O), fluorine (0.9–1.4 wt.% F), Rb (1400–1830 ppm), and Cs (200–250 ppm). In contrast, the aplite/pegmatite sheets are rich in silica (72.1–76.3 wt.% SiO_2) and potassium (mostly >5 wt.% K_2O), but poor in sodium (1.9–2.9 wt.%

304 Na_2O), lithium (<0.03 wt.% Li_2O), fluorine (0.2–0.64 wt.% F), Rb (356–755 ppm), and Cs (17–33
305 ppm). High-field strength trace elements (HFSE) are highly variable in their concentrations: Sn (13–80
306 ppm), W (4–46 ppm), Nb (17–69 ppm), Ta (6–50 ppm), and Zr (9–29 ppm). The chemical
307 composition of the "complex sheets" usually lies between the "granites" and "aplite-pegmatites".
308 Within the WR data, there is a strong positive correlation between Li, Rb, F, and Na (i.e. elements
309 hosted in Li-mica and albite), and among all these elements and the Mn/Fe value. All rock types,
310 excluding biotite granite, have very low contents of all REEs, flat REE distribution pattern, and a
311 distinct tetrad effect (Fig. 7e). The extremely low REE-content of the sample 4963 probably indicates
312 strong interaction with a late- or post-magmatic fluid. The biotite granite has an REE pattern typical of
313 common granitoids with a relative enrichment of LREE over HREE. The granites and sheets from
314 Megiliggar show an extreme enrichment in Li, Nb, Ta, Sn and W relative to other Cornubian granites,
315 and show significantly lower Zr and REE (e.g. Chappell and Hine, 2006; Müller et al., 2006; Simons
316 et al., 2016, 2017).
317 The biotite granite differs from all the above mentioned rock types in being slightly enriched in FeO_{tot}
318 (1.37 wt.%), MgO (0.26 wt.%) and strongly enriched in U (39 ppm), Th (7 ppm) and all REEs (for
319 example Ce 25 ppm).
320
321 **6. Minerals**
322 **Quartz** typically has consistent primary abundances of trace elements and therefore gives reliable
323 information about the composition of the magma from which it crystallized (e.g. Jacamon and Larsen,
324 2009). The chemical composition of quartz in samples from Megiliggar is characterized both by a
325 relatively large scatter of trace elements in each sample, and, conversely, by similarity in composition
326 across all samples (Fig. 8, Supplementary Table 3). Surprising is the strong positive correlation
327 between Ti and Al, which is very different to the usual negative correlation between these elements in
328 common granites, with Ti decreasing with increasing Al during fractionation (Müller et al., 2010;
329 Breiter et al., 2014). The Al/Ti ratio, usually a good indicator of magma fractionation, has a narrow
330 interval of 10–40. Quartz from all samples is very rich in Li, but poor in Ge. In comparison with a
331 large dataset for Variscan granites and pegmatites (Breiter et al., 2013, 2014), quartz from the MSC

shows trace element trends which are more like those of granites than pegmatites. Indications of a hydrothermal origin, low contents of Ti (<5 ppm) coupled with very high Al (>>1000 ppm) (Rusk et al., 2008) were not found.

K-feldspar (Kfs) is present in two textural varieties: (i) as perthite which appears in rock facies with typical pegmatite textures, usually enriched in schorl, and (ii) as small phenocrysts (<25 mm) in the Tregonning Granite. Homogeneous Kfs, often with abundant inclusions of albite (but not admixtures), prevails in other rock types (groundmass in the Tregonning Granite, leucogranite sheet, aplites). In layered rock, the tourmaline-rich sample #4965 contains only homogeneous Kfs, while sample #2015 contains perthite in the layer #4 and homogeneous Kfs in all other layers.

Chemically, two groups of K-feldspars may be distinguished (Supplementary Table 4): (i) relatively more evolved P-enriched (>0.3 wt.% P_2O_5) grains with 0.2–0.6 wt.% Rb_2O were found in the granites (incl. biotite granite from Legereath Zawn) and complex sheets, and (ii) less evolved crystals, with P_2O_5<0.3 wt.% and Rb_2O<0.3 wt.%, in the aplite-pegmatites. The abundance of P and Rb does not relate to whether the K-feldspar has a homogeneous or perthitic texture.

Albite is the main plagioclase phase containing less than 1.2 wt.% CaO (<0.06 apfu Ca, Supplementary Table 2), in line with previous studies (Stone, 1992; Simons et al., 2017). The highest content of Ca was found in albite from the biotite granite dyke (0.47–1.18 wt.% CaO), while nearly all grains from the other rock types contain albite with <0.4 wt.% CaO. The Li-mica bearing complex sheets contain P-enriched albite (0.4–0.6 wt.% P_2O_5, 0.015–0.022 apfu P), while albite from the Tregonning Granite and from the tourmaline-bearing facies of the sheets usually contains less than 0.1 wt.% P_2O_5 (<0.004 apfu P).

Micas usually form small grains (<1 mm across) that are evenly distributed through the samples. Aggregates of larger muscovite flakes were only found in some thin laminae within complex sheets, e.g. layer #9 in sample 2015 (Fig. 4), and layer #6 in sample 4965 (Fig. 5). Three types of mica can be distinguished in the rocks studied: (i) zinnwaldite-trilithionite group (hereafter “lepidolite”), (ii) muscovite-phengite group (hereafter “muscovite”), and (iii) mica slightly enriched in Li within the siderophyllite–muscovite-zinnwaldite space (hereafter “Li-Fe-Al-mica”). This mica subdivision is represented on binary plots of mineral composition (Fig. 9a, b).

Lepidolite dominates in granites (e.g. outcrops of the Tregonning Granite and leucogranite sheets) and has also been found in the complex sheets. It is rich in Li (4–5 wt.% Li_2O), Rb (0.8–1.1 wt.% Rb_2O) and F (7.8–9 wt.% F) (Supplementary table 5); all these elements show a positive correlation. Muscovite is present in complex sheets and dominates in aplite-pegmatites. It is enriched in Fe (typically containing 2 wt.% FeO, occasionally up to 4 wt.%), but poor in Li, Rb and F (<0.1 wt.% Li_2O, <0.2 wt.% Rb_2O, <0.1 wt.% F). In the fine-layered parts of complex sheets, muscovite and lepidolite micas alternate (Fig. 9c).

"Li-Fe-Al-mica" was found dominantly in the biotite granite dyke and occasionally also in the complex sheets. Macroscopically, this mica is black, resembling common biotite, which strongly differs from the light beige to pink colour of zinnwaldite–trilithionite. In comparison to the Li-micas of the zinnwaldite-trilithionite series, this mica is lower in Li (0.8–2.15 wt.% Li_2O), Rb (0.3–0.6 wt.% Rb_2O) and F (3–4 wt.% F) and strongly variable in Al and Fe (22–31 wt.% Al_2O_3, 4–18 wt.% FeO), with an approximate mean formula of $K_2Li_{1.6}Fe_1Al_{2.7}(Si_6Al_2O_{20})F_{1.5}(OH)_{2.5}$.

Of the trace elements, Cs is mainly present in lepidolite (500–6000 ppm, Supplementary table 6), whilst it does not exceed 100 ppm in muscovite and Li-Fe-Al-mica. Similarly, Ta (Fig. 9d) and W have a positive correlation with Li, reaching 25–75 ppm Ta and 300–600 ppm W in lepidolite from the Tregonning Granite and leucogranite sheet. Conversely, the highest content of Sn was found in muscovite from the complex sheets (180–340 ppm) and the highest Nb in the Li-Fe-Al-mica from the biotite granite dyke (120–350 ppm, Fig. 9e). Micas are the major host of Cs and W in all Megiliggar rocks, while their importance for the Sn-, Nb-, and Ta-budget of the rock is limited, consistent with the findings for topaz granites across the region (Simons et al., 2017).

Tourmaline was found, with variable modal abundances, in all examined varieties of granite and sheet rocks. It forms elongate grains less than 1 mm long in granites and aplites, but also up to 5–10 cm long and 1–2 mm wide thin needles in pegmatites. Higher abundances of tourmaline were found in rock types and laminae relatively rich in K-feldspar and muscovite, while samples relatively enriched in albite and lepidolite are usually tourmaline-poor. The tourmaline is mainly schorl and more rarely foitite (Fig. 10a). The most Li-rich tourmaline, which was found in the leucogranite sheet is dark green in colour, contains up to 0.7 apfu F (Supplementary table 7, Fig. 10b). Li is likely to occupy the Y-site

in the following proportions: $\square_{0.1}Li_{0.7}(Fe+Mg+Mn)_{1.2}Al_1$ apfu (Fig. 10c). This tourmaline is alkaline and poor in vacancies; it should be termed Li-rich fluor-schorl. Tourmaline in other rocks is mostly black Li-F-poor schorl up to F-poor foitite. Tourmaline in the Tregonning Granite is usually zoned with relatively F-Na-Al-Mn-rich and Fe-Mg-depleted rims. These data are consistent with previous studies (London and Manning, 1995; Duchoslav et al., 2017).

In the finely banded rock domains (both #2015 and #4965), the contents of Fe, Mn, and Na in tourmaline increase, while Mg, Ca, and vacancies decrease from the oldest to the youngest layers. Some crystals are slightly zoned, often with schorl cores and slightly Li-F-enriched rims.

Schorl crystals with quartz cores were found in some aplite/pegmatite sheets in the central part of the MSC (see images in the Supplementary material). Similar textures have been described from Roche Rock, St. Austell (Müller et al., 2005). This tourmaline is slightly chemically zoned (with relatively Fe-rich and Mg-poor rims), but is generally low in Li and F. The Li and F contents of tourmaline generally show a positive correlation with those in mica.

Among the trace elements (Supplementary table 8) in the tourmaline, Sn correlates strongly with Li reaching 60–130 ppm in fluor-schorl from the leucogranite sheet (Fig. 10d), and Ta attains 5–8 ppm in the leucogranite sheets. In contrast, the concentrations of W and Nb are generally very low: <0.5 ppm and <5 ppm, respectively, consistent with recent studies by Duchoslav et al. (2017) and Simons et al. (2017). Niobium and Ta in tourmaline, as in micas, are decoupled: Ta is preferentially enriched in fluor-schorl from the leucogranite sheets and in schorl from the youngest layer #6 in the fine-layered aplite #4965, while Nb prevails in tourmaline from all other locations. Levels of Zn in tourmaline vary mostly between 400 and 600 ppm with some outliers down to 150 and up to 700 ppm, but with little systematic difference between rock types. Gallium concentrations are highly variable (70–350 ppm), with the highest concentrations (>200 ppm) found in tourmaline from the leucogranite sheets and in the latest layer #6 of the sample #4965. The concentration of Be is usually <10 ppm, except in tourmaline from leucogranite sheets where it reaches 30–50 ppm. Contents of Cs, Ge and In are low in tourmaline from all rock types: <3 ppm, <5 ppm, <1 ppm, respectively.

Fluoroapatite appears to have crystallised relatively late in all rock types as it is interstitial and anhedral. Apatite is enriched in Mn in the granites, reaching 0.2–0.3 apfu, and in the albite-rich

laminae of the layered rocks, with up to 0.52 apfu Mn (7.18 wt.% MnO). Amblygonite, which shows limited alteration to montebrasite along cleavage planes, was found occasionally in the leucogranite sheets as aggregates of anhedral grains several mm across. Monazite and xenotime form scarce small grains (usually ~20 μm, occasionally up to 100 μm) in all rock types. They are the major carriers of REE.

Rutile forms small anhedral grains which show irregular or patchy zonation (in SEM-BSE mode) and contain inclusions of columbite, ixiolite or tantalite (Fig. 11a,b,c). Rarely, intergrowths of rutile and cassiterite were found (Fig. 11d). Rutile, which is enriched in W and slightly in Nb (up to 6.1 wt.% WO_3 and 1.6 wt.% Nb_2O_5), was often found as inclusions in micas in the biotite granite dyke. It is the only Nb, W-bearing mineral in this rock. Rutile, which is strongly enriched in Nb and Ta (up to 17 wt.% Nb_20_5, 36 wt.% Ta_2O_5), and appears together with Fe-columbite in the Tregonning Granite, complex sheets and aplite-pegmatites (Fig. 12a), locally contains up to 0.7 wt.% Sc_2O_3 and 1 wt.% WO_3 (Supplementary table 9).

Columbite-group minerals form 100–200 μm long needle-like crystals (Fig. 11e, f) or smaller (<30 μm) anhedral inclusions in rutile (Fig. 11a, c). They typically have a Ta/(Nb+Ta) ratio <0.5, i.e. the mineral can be classified as **columbite.** The Mn/(Fe+Mn) value strongly varies not only among samples, but also within a single grain. Generally, columbite-Mn is more common in the granites and complex sheets, while columbite-Fe prevails in aplite-pegmatite sheets (Fig. 12b). Fe-columbite contains 0.5–1 wt.% Sc_2O_3 and 2–10 wt.% WO_3. Columbite-like grains with >10 wt.% WO_3 (up to 30.7 wt.% WO_3) are classified as "**ixiolite**", however it is difficult to confirm this without more crystal-chemical information. The W-rich grains (domains in complex grains) are relatively Nb- and Fe-rich (Figs. 12b, c). **Tantalite-Mn** was found only as one small crystal included in rutile in the Tregonning Granite (Fig. 11b).

Cassiterite occurs as scarce subhedral grains in complex sheets (#5304), locally associated with rutile (Fig. 11d). It is poor in minor elements (>97.8 wt% SnO_2) containing only traces of Nb and Fe.

Wolframite forms small (≈20 μm) anhedral grains in some samples from complex sheets (#2015, 5304). It is poor in minor elements (usually <1 wt.% Nb_2O_5+Ta_2O_5+Sc_2O_3), with only one grain containing 4.3 wt.% Nb_2O_5, 2.6 wt.% Ta_2O_5 and 1 wt.% SnO_2.

Monazite and **xenotime** (Fig. 11g), major hosts of REE, are scarce, but were found in all rock types. **Uraninite**, which forms both euhedral and anhedral grains up to 50 μm across, is quite common and is usually rimmed by **pyrite** (Fig. 13h, i). Within the finely banded aplite (#4965) it was found as inclusions in columbite and zircon (Fig. 11j).

Zircon is a rare accessory mineral in all rock types, as indicated from low WR Zr values, but rare euhedral grains, 10-20 μm across, were found in all samples (Fig. 11f). Numerous inclusions of uraninite were found in some zircon grains from the fine-layered aplite (Fig.11j, k). Zircon is relatively poor in trace elements (usually Y_2O_3<0.6 wt.%, Yb_2O_3<0.3 wt.%, ThO_2<0.3 wt.%, Supplementary table 10), with unique values of 5.46 wt.% UO_2, 0.40 wt.% ThO_2, 1.89 wt.% Y_2O_3 and 0.49 wt.% Yb_2O_3 (Fig. 13). Hf contents are highly variable, ranging from 1.5–8.9 wt.% HfO_2 (0.013–0.082 apfu Hf); the highest values were found within the rims of some crystals from the leucogranite sheets (Fig. 11k). Zircon from the aplite-pegmatite sheets has generally lower Zr/Hf values and lower contents of trace elements than zircon from the complex sheets (Fig. 13). Zircon from the biotite granite dyke is chemically uniform having intermediate Zr/Hf values (≈50) and low contents of all trace elements. All zircon types are free of the "ore elements" Nb, Ta, W, Bi, and Cu. Magmatic **fluorite** was found occasionally in some finely banded rock samples. Sulphides (**arsenopyrite** (Fig. 11l**)**>> **sphalerite, galena, bismuthinite**, **molybdenite**) and **native Bi** were found in some aplite-pegmatite sheets.

7. Discussion

The origin of layered albite-pegmatite sheets, which can include finely-banded aplites (line rock, Schaller, 1925), is an intriguing petrogenetic question which has broad implications for the genesis of pegmatites. Sheets containing fine-grained "aplitic" (usually in the lower half) and coarse-grained "pegmatitic" textures (usually in the upper half) have been explained previously as having both metasomatic (Schaller, 1925; Stone, 1969), and magmatic origins (Jahns and Tuttle, 1963; Webber et al., 1997; London, 2014). The MSC exposures at Megiliggar Rocks provide an excellent locality for testing these hypotheses. Our discussions focus on the relationship between the sheets and the nearby Tregonning Granite, mainly whether the sheets were formed from relatively evolved melt segregations

within the roof of the Tregonning Granite. Differentiation of initially homogeneous granitic melt to Na-Li-F- and K-B-enriched portions was the main process determining the diversity of sheet rocks. This Na-Li-F vs. K-B differentiation was manifested at two scales: (i) between the Tregonning Granite and MSC; and (ii) within the aplite-pegmatite banding of individual sheets.

7.1 MSC rocks as fractionated equivalents of the Tregonning Granite; large-scale Na-Li-F vs. K-B differentiation

All previous authors agree unequivocally that there is a link between the Tregonning Granite and the MSC. Hosking (1952) interpreted the MSC as having a purely magmatic origin, with aplite and pegmatite sheets (including layers or laminae in the sheets) forming by repeated injections of the same primary magma which varied episodically in its water and volatile contents. Later, Stone (1969, 1975, 1992) proposed a combination of magmatic and metasomatic processes, with initial formation of the aplites by crystallisation of residual melts from the Tregonning Granite, followed by subsolidus metasomatic recrystallization of the aplites to pegmatites and replacement of albite by K-feldspar. This view was based on the observation that the aplitic parts of the sheets were more mineralogically and chemically similar to the Tregonning Granite than the pegmatitic portions. The development of banded aplite-pegmatite sheets has also been interpreted to be a consequence of repeated melt decompression during fracture propagation accompanying xenolith separation (Bromley and Holl, 1986; Bromley, 1989). During decompression, volatile exsolution drove the residual melt towards the solidus, resulting in rapid nucleation and crystallization of aplite; the exsolved hydrous fluid trapped above the aplite contributed to the development of a complementary pegmatite layer.

From our textural and chemical data we suggest a dominantly magmatic origin for all MSC rock types; however, interpretation of the WR chemical data is not straightforward. Nevertheless, the Na vs. K differentiation, mineralogically expressed in albite vs. K-feldspar enriched domains is well documented. In an eastwards traverse from the margin of the Tregonning Granite, through the leucogranite sheets and complex sheets to the aplite-pegmatite sheets, there are conspicuous changes in some major and trace element concentrations (Table 1): Na_2O decreases from 3.3–4.3 to 1.9–2.9 wt.%, F decreases from 0.9–1.4 to 0.2–0.6 wt.%, Li_2O decreases from 0.23–0.41 to 0.01–0.03 wt.%,

Rb decreases from 530–1830 ppm to 360–760 ppm, and Cs from 88–253 ppm to 17–33 ppm. In contrast, K_2O in the same direction increases from 3.3–4.5 to 3.5–6.1 wt.%. The concentration of B, as evident from the abundance of tourmaline, also increases eastwards, but chemical data for this element are not available. The contents of Si, Al, Fe and P remain fairly constant, and the HFSE are variable but show no obvious trends.

According to the K/Rb ratio, the most common index for magmatic fractionation, the leucogranite sheets (K/Rb=19) are more evolved than the Tregonning Granite (K/Rb=31), which is consistent with their interpretation as a product of crystallization of residual melt sourced from the Tregonning Granite roof zone. The lepidolite-bearing complex sheets show K/Rb values only slightly higher than the leucogranites (K/Rb=30–44), and have slightly lower contents of Li, Rb, and F, indicating that they may also represent fractionated equivalents of the Tregonning Granite melt, notwithstanding fracture-controlled partial escape of Li-F-bearing fluids into the surrounding host rocks. Conversely, the chemical composition of tourmaline-muscovite dominated aplite-pegmatite sheets is less evolved than the Tregonning Granite having relatively low Rb-contents (high K/Rb=58–94) and extremely low F, Li, and Cs abundances.

The complex sheets and aplite-pegmatite sheets have highly variable mobile alkalis and fluorine compositions. Lower contents of the rare alkalis in the distal parts of the sheet system may be explained by variable fluid escape from the crystallizing melt. Enrichment of the Mylor Slate Formation in the exocontact, previously noted by Stone and Awad (1988), may have been controlled by fractures now represented by steeply dipping aplite/pegmatite sheets (Fig. 2g). However, this does not explain the relative B enrichment in the distal aplite-pegmatite sheets. In the proximal part of the MSC (Fig. 1b), both Li-F-bearing tourmaline and mica crystallized late in the leucogranites, due to low levels of Fe in the melt. In the middle part of the MSC, in the complex sheets, crystallization of tourmaline precedes the crystallization of Li-F-micas. Tourmaline was the first Fe-bearing mineral in which the melt became saturated; this demonstrates a relatively high abundance of B and Fe in the melt at the beginning of the crystallization. Mica crystallized later, when F was sufficiently concentrated in the residual melt. In the distal MSC, within the aplite-pegmatite sheets, B predominates over F, even though its fluid/melt partition coefficient is distinctly higher than that of

fluorine. Thus, the eastwards proximal to distal decrease in F was not a result of its partitioning into a fluid and escape to the slates, but a consequence of its consumption by the relatively late crystallization of F-minerals (topaz?) in the proximal and central parts of the MSC. The last portion of melt, filling the distal parts of the sheet system, was F-poor, but still had sufficient B for tourmaline saturation, with Fe scavenged from the slate host rocks.

Variations in Nb- and Ta-contents and Nb/Ta ratios are often used as indicators of the degree of granite and pegmatite melt evolution and/or zoning (Ballouard et al., 2016). Tantalite has a higher solubility in peraluminous granite melts at low temperature relative to columbite (e.g. Linnen and Keppler, 1997), which commonly results in the melt evolving from Fe–Nb- to Mn–Ta-enriched end-members of the columbite group (Černý et al., 1985; London, 2008). Moreover, the crystallisation of micas also aids in the decoupling of Nb and Ta within a peraluminous melt, with Nb preferentially partitioning into biotite compared with Ta; the latter is strongly partitioned into residual F-bearing melts (e.g. Stepanov and Hermann, 2013). Nevertheless, changes in the Nb/Ta ratio are also influenced by a succession of coprecipitating minerals (oxides, micas, tourmaline) and the combined effects of Li, Na, B, F, and P in the melt or fluid phase (e.g., Johan and Johan, 1994; Belkasmi et al., 2000; Novák et al., 2003; Van Lichtervelde et al., 2006; Wise et al., 2012). In the MSC, fluorine presumably remained in pockets of residual melt until the crystallisation of topaz (e.g. Figs. 4, 5), with Ta therefore concentrated within the last layers to crystallise, while Nb is more evenly distributed throughout the rocks. However, in examining larger volume WR samples (Figs. 14a, b), the Nb/Ta ratio is scattered between 1–7 independent of rock type and Li- and F-content. In micas and tourmaline (Figs. 14c-f) the Nb- and Ta-contents and the Nb/Ta ratio are highly variable within individual samples, but the general trend is to relative Ta-enrichment in Li-enriched grains and/or the outer zones of crystals. We conclude that WR Nb/Ta ratios in Megiliggar rocks were controlled by the order of crystallization and relative amounts of oxides vs. silicate carriers and, in this case, can not serve as a marker of melt fractionation.

The mineralogy of the different MSC rock types reflects their WR compositions, with the leucogranite sheets and complex sheets containing lepidolite, relatively high P-contents in both feldspars and Rb in K-feldspar, and higher Li and Fe/Mg in tourmaline. These signatures are characteristic of “evolved” or

556 "highly fractionated" rocks, comparable with peraluminous tin granites in the Erzgebirge (Förster et
557 al., 1999; Breiter et al., 2005) and France (Raimbault et al., 1995), and LCT pegmatites (London,
558 2008). In contrast, the aplite-pegmatite sheets, which contain Li-F-poor muscovite, and often schorl,
559 are chemically and mineralogically more primitive. However, all rock-types show nearly identical and
560 low (12–21) WR Zr/Hf values, which are generally indicative of high degrees of fractionation
561 (Hanchar and Hoskin, 2003; Breiter and Škoda, 2017). The zircon Zr/Hf value (Fig.13) is consistent
562 with WR Zr/Hf data and zircon from the aplite/pegmatite sheets is at least as strongly differentiated as
563 zircon from the complex sheets and is more fractionated than zircon from the Tregonning Granite.
564 The field relations and geochemical similarity indicate a direct link between the Tregonning Granite
565 and the MSC. The textural and mineral diversity in the sheets, from proximal to distal, eastwards
566 across the study area, was caused by Na-Li-F vs. K-B fractionation, where the K-B-rich portion of
567 melt (fluid) could migrate more effectively to the distal part of the crystallizing magmatic system.
568 However, the Zr/Hf value, unaffected by this fractionation, is similar across the whole MDC,
569 demonstrating a uniform magmatic source.
570 The composition of the biotite granite dyke is distinctive and does not follow the aforementioned
571 trends; this lithology does not appear to form part of the MSC. Instead, it is likely to be an expression
572 of earlier magmatism petrogenetically linked to the Godolphin Granite (two mica) or biotite granite
573 porphyry ('elvan') dykes (see Simons et al., 2016).
574 The suggestion that the easternmost distal expression of the MSC is represented by quartz veins linked
575 directly to aplite-pegmatite sheets (Hosking, 1952; Badham, 1980; Bromley, 1989) is refuted; we think
576 that this assertion was based on miscorrelation of the easternmost MSC sheets with pre-granite
577 subhorizontal quartz veins contained within the S3 cleavage. The similar orientation of the MSC
578 sheets and these quartz veins reflects the influence of the mechanical anisotropy imparted by the S3
579 cleavage on the propagation of fractures controlling emplacement of the MSC.
580
581 **7.2 Local Na-Li-F vs. K-B fractionation within layered sheets**
582 The complex sheets and aplite-pegmatite sheets within the MSC differ from the majority of common
583 pegmatite sheets having a more complex structure, often appearing to have formed as a result of

584 multiple melt injections. The banding almost certainly originated via *in situ* fractionation, as crystals
585 grew upwards; in combination with the emplacement of younger narrow melt injections which
586 crystallized from both contacts inwards (compare Hosking, 1952). This feature was encountered in
587 both complex sheets and aplite-pegmatites. Crystallization within most single sheets (or sheet
588 domains), i.e. formed from a single injection of melt, is comparable with other examples of pegmatite
589 sheets (Weber et al., 1997; London et al., 2012).
590 Samples #4965 and #2015 represent parts of *in situ* crystallized layered sequences, at an appropriate
591 layer scale for detailed investigation. Sample #4965 (Fig. 5, Supplementary table 2) represents a fine-
592 grained (aplitic) part of an aplite-pegmatite sheet which is albite-poor and dominated by quartz, K-
593 feldspar, muscovite and tourmaline. The composition of individual laminae can be traced effectively
594 from the Qtz–Kfs ratio, but without any general evolutionary trend (Fig. 15a). The abundance of
595 tourmaline varies between 4.1–9.8 vol.% (ca. 0.4–1.0 wt.% B_2O_3). The younger laminae #4→6
596 contain 1–2 vol.% apatite (up to 1 wt.% P_2O_5). The melt, from which layers #1→5 crystallized, was B-
597 and P-rich, but relatively F-poor (<0.15 wt.%), and only the youngest lamina #6 reaches nearly 5 wt.%
598 F due to crystallization of common topaz from the residual liquid or from a new injection of F-rich
599 melt/fluid. In any case, the crystallised rock composition lies away from the granite minima (Johannes
600 and Holtz, 1996, Fig. 15b).
601 Sample #2015 (Fig. 4, Supplementary table 1) represents a finely banded portion of a Li-F-bearing
602 complex sheet. Its mineral composition is more complex than in the previous case, with bands
603 dominated by K-feldspar, tourmaline and muscovite alternating with those strongly enriched in albite
604 and zinnwaldite. The oldest portion of the layered sequence, lines #1→7, evolved systematically from
605 a Qtz-Kfs-rich composition towards the Ab-apex of the Qtz-Ab-Kfs diagram (16→72 wt.% Ab, Figs.
606 4, 15a). The bands have variable compositions, but the general trend towards Ab-enrichment is
607 obvious. The computed volatile content varies between 0→1.6 wt.% B_2O_3, 0.2→0.8 wt.% P_2O_5, and
608 0.1→2.4 wt.% F. Although B generally decreases along this trend, P levels remain unchanged and F,
609 Li and Rb increase (Fig. 9c). Here, it should be noted that the sample does not really represent the
610 mean of the whole banded sheet, but only a partial section; the real composition of the injected melt
611 may be different.

612

613 **7.3 Comparison with similar aplite-pegmatite sheets**

614 The first model for the generation of layered aplite-pegmatite sheets was developed by Jahns and
615 Tuttle (1963), which was based on a study of miarolitic pegmatites in San Diego County, California.
616 The authors described a typical arrangement of "sodic aplite" in lower, and "potassic pegmatite" in the
617 upper parts of horizontal sheets with inward crystallization of both facies which finished in the central
618 pocket zone. Later, London et al. (2012) and London (2014) confirmed the common position of (often
619 layered) aplitic domains in the lower part, and pegmatitic domains in the upper part of many
620 horizontal pegmatite sheets, but questioned their dominantly sodic vs. potassic character. Another,
621 rhythmic style of layering, expressed as alternations of 0.5–2 m thick K-feldspar and tourmaline-
622 dominated pegmatite and albite-rich aplite layers, has been reported from the B-rich Calamity Peak
623 layered pluton (Duke et al., 1992).
624 The evolution of the banded sequences in the MSC is comparable with the George Ashley Block
625 (GAB) pegmatite, Pala district, California (Weber et al., 1997). The mean composition of the granite
626 sheet and complex sheets from Megiliggar is only slightly Ab-enriched in comparison with the mean
627 of the GAB pegmatite, which may be explained by a higher content of F in the Megiliggar sheets (Fig.
628 15b). The composition of the oldest band in the sample #2015 and the WR #4965 is nearly identical to
629 the composition of the K-rich portions of the GAB pegmatite, located in its central-upper parts, while
630 the mean of the late fine-layered portion of sample #2015 is equal to the composition of the finely
631 banded aplitic portion of the GAB pegmatite (Webber et al., 1997; Fig. 15b). Therefore, the banded
632 portions of the MSC we have studied experienced the same differentiation as the whole George
633 Ashley Block pegmatite dyke. In both localities, both contrasting rock facies (Na+F+Li vs. K+B-
634 enriched) are adjacent in a single sheet, together having logically expected compositions near the
635 "granitic minimum" of a slightly B-, resp. F-enriched melt (Manning, 1981; Pichavant, 1987; Fig.
636 15b).

637 Weber et al. (1999) and London et al. (2012) concluded that crystallization of finely banded aplite
638 ("line rock") to give a water- and fluxes-poor mineral assemblage near the lower contact of the sheets

639 was likely due to undercooling, whereas accumulation of volatiles in the upper parts of the sheet
640 decreased the degree of undercooling and promoted crystallization from a flux-enriched boundary-
641 layer, i.e. crystallization of rare minerals and grainsize coarsening. At Megiliggar, this process is
642 expressed in complex sheets which show a transition from muscovite-bearing aplite through to Li-F-
643 mica-bearing aplite to coarse-grained sheet domains bearing Li-F-mica and tourmaline. In the aplite-
644 pegmatites, the increase in F and Li during crystallization of the aplitic unit was minimal, but their
645 influence was superseded by increasing abundances of water and boron. Repeated sudden
646 decompression followed by exsolution of fluid driving such grainsize changes might be driven by
647 repeated fracture propagation during the lateral growth and inflation of the MSC (Weber et al., 1997;
648 London, 2008) rather than xenolith separation (Bromley and Holl, 1986; Bromley, 1989). In such
649 conditions, the growth rate of K-feldspar is higher than that of quartz and albite (Swanson, 1977): this
650 is well demonstrated in layers 1→7 of sample #2015, although the initial dominance of K-feldspar was
651 superseded, in a stepwise fashion, by albite. Similar, although not so significant, is the evolution in
652 lines 11→13, 15→17 and 20→22.

653

654 **7.4 Possible implications for models of pegmatite genesis**

655 Among recent models for the genesis of pegmatites, the complex model by London (for example
656 London, 2008, 2014) and model based on the study of melt inclusions by Thomas (for example
657 Thomas et al., 2006; Thomas and Davidson, 2012, 2013) are the best constrained and often discussed,
658 including mutual discussion of both authors (London, 2015; Thomas and Davidson, 2015). In a very
659 simplistic way, London explained the specific features of pegmatites as crystallisation products of
660 peraluminous water-undersaturated melts via the boundary layer effect, while Thomas and Davidson
661 prefer crystallization from immiscible hydrous peralkaline melt. Detail discussion of the mentioned
662 models is beyond the scope of this article, but we would like to stress the importance of our findings
663 from Megiliggar, which we feel should be considered in any future models for pegmatite genesis.

664 The evidence from outcrops at Megiliggar, and our detail mineralogical studies, suggests an intimate
665 coexistence of "granite", "aplite" and "pegmatite" rocks of similar mineral and chemical composition,
666 differing only in grain size and texture. We did not find any evidence of abrupt changes in mineral and
667 chemical composition, though sudden changes in texture, from pegmatitic to aplitic varieties, and vice
668 versa, are common. In other words, an evolved peraluminous granitic melt may repeatedly change in
669 its style of crystallization from granitic to aplitic and pegmatitic without any abrupt changes in
670 chemical or mineral composition. The factors controlling granitic or pegmatitic styles of evolution
671 (water and volatile contents? undercooling? fluctuation of pressure?) changed gradually, smoothly,
672 are were reversible.

673

674 **8. Conclusions**

675 Chemical and mineralogical data together with a gradual change in prevailing textures suggests a
676 strong genetic link between the Tregonning Granite and MSC. The lithologies within the MSC formed
677 from residual melt escaping from the Tregonning Granite. This melt was strongly peraluminous and,
678 in comparison with other Cornish granites, rich in F, Li, Rb, Cs, Sn, W, Nb, Ta, and U, and poor in Fe,
679 Mg, Ca, Sr, Th, Zr, and REE.
680 During crystallization, the melt underwent differentiation into Na-Li-F-enriched vs. K-B-enriched
681 domains, which may be traced at two scales: (i) in finely banded sequences where the K-B-enriched
682 layers evolved into more Na-Li-F-enriched ones, and (ii) generally, the Na-Li-F-enriched proximal
683 leucogranite sheets pass gradually into K-B-dominated distal aplite-pegmatites. The mean composition
684 of the sheets is similar to the eutectic composition of leucocratic granitic melts saturated in water and
685 slightly enriched in F and B. Differentiation to fine-grained (i.e. aplitic) and coarse-grained (i.e.
686 pegmatitic) layers was most probably forced by repeated decompression and undercooling due to
687 fracture propagation during the lateral growth and inflation of the MSC system.
688 With distance from the contact with the parental Tregonning Granite, the melt became depleted in the
689 fluxing and volatile elements F, Li, Rb, and Cs, probably due to escape of fluid to surrounding slates

or via fractures, but the Zr/Hf value in all rock types remains virtually unchanged indicating derivation from a single parental magma source.

Knowledge gained at Megiliggar Rocks may help to better understand the chemical and mineralogical evolution of large aplite-pegmatite systems and their relation to parental granite plutons. Mineral and textural zoning, usually evolving from the contacts to the core of the pegmatite bodies, is at Megiliggar combined with a lateral transition from dominantly granitic to aplitic and pegmatitic textures, chemically expressed in Na-F-Li vs. K-B differentiation. The combination of transversal and longitudinal zoning in the Megiliggar sheets may provoke similar studies in other well-exposed aplite-pegmatite systems.

Acknowledgements

Laser-ablation ICP-MS analyses of micas and tourmaline in Masaryk University Brno were supported by the Czech Science Foundation project No. GA14-13600S. All other analytical work for this contribution was supported by the RVO 67985831 in the Institute of Geology of the Czech Academy of Sciences, Praha. We are grateful to P. Davidson and an anonymous referee for their reviews.

References

Alexander, A.C., Shail, R.K., 1996. Late‐to post‐Variscan structures on the coast between Penzance and Pentewan, south Cornwall. Proceedings of the Ussher Society, 9 72–78.

Autunes, I.M.H.R., Neiva, A.M.R., Ramos, J.M.F., Silva, P.B., Silva, M.M.V.G., Corfu F., 2013. Petrogenetic links between lepidolite-subtype aplite-pegmatite, aplite veins and associated granites at Segura (central Portugal). Chemie der Erde 73, 323–341.

Badham, J.P.N., 1980. Late magmatic phenomena in the Cornish batholith – useful field guide for tin mineralization. Proceedings of the Ussher Society 5, 44–53.

Ballouard, C., Poujol, M., Boulvais, P., Branquet, Y., Tartese, R., Vigneresse, J-L., 2016. Nb-Ta fractionation in peraluminous granites: A marker of the magmatic-hydrothermal transition. Geology 44, 231–234.

Belkasmi, M., Cuney, M., Pollard, P.J., Bastoul, A., 2000. Chemistry of the Ta-Nb-Sn-W oxide minerals from the Yichun rare metal granite (SE China): genetic implications and comparison with Moroccan and French Hercynian examples. Mineralogical Magazine 64, 507–523.

Breaks, F.W., Moore, J.M.Jr., 1992. The Ghost Lake batholith, Superior province of northwestern Ontario: a fertile, S-type, peraluminous granite – rare-element pegmatite system. Canadian Mineralogist 30, 835–875.

Breiter, K., Ackerman, L., Svojtka, M, Müller, A., 2013. Behavior of trace elements in quartz from plutons of different geochemical signature: A case study from the Bohemian Massif, Czech Republic. Lithos 175–176, 54–67.

Breiter, K., Ackerman, L., Ďurišová, J., Svojtka, M., Novák, M., 2014. Trace element composition of quartz from different types of pegmatites: A case study from the Moldanubian Zone of the Bohemian Massif (Czech Republic). Mineralogical Magazine 78, 703–722.

Breiter, K., Müller, A., Leichmann, J., Gabašová, A., 2005. Textural and chemical evolution of a fractionated granitic system: the Podlesí stock, Czech Republic. Lithos 80, 323–345.

Breiter, K., Müller, A., Shail, R., Simons, B., 2016. Composition of zircons from the Cornubian Batholith of SW England and comparison with zircons from other European Variscan rare-metal granites. Mineralogical Magazine 80, 1273–1289.

Breiter, K., Škoda, R., 2017. Zircon and whole-rock Zr/Hf ratios as markers of the evolution of granitic magmas: Examples from the Teplice caldera (Czech Republic/Germany). Mineralogy and Petrology 111, 435–457.

Bromley, A. V., 1989. Field guide - the Cornubian orefield. 6th International Symposium on Water-Rock Interaction, Malvern (UK). International Association of Geochemistry and Cosmochemistry, Camborne School of Mines, UK. pp. 111.

Bromley, A.V., Holl, J. 1986. Tin mineralisation in southwest England. In: Wills, B.A., Barley, R.W. (eds) Mineral processing at a crossroads, NATO ASI Ser. No.117. Martinus Nijhoff, Dordrecht, 195–262.

Černý, P., 1991. Fertile granites of Precanbrian rare-element pegmatite fields: is geochemistry controlled by tectonic setting or source lithologies? Precambrian Research 51, 429–468.

745 Černý, P., Meintzer, R.E., Anderson, A.J., 1985. Extreme fractionation in rare-element granitic
746 pegmatites: selected examples of data and mechanisms. Canadian Mineralogist 23, 381–421.
747 Chappel, B.W., Hine, R., 2006. The Cornubian Batholith: an example of magmatic fractionation on a
748 crustal scale. Resource Geology 56, 203–244.
749 Charoy, B., 1986. The genesis of the Cornubian Batholith (South-West England): the example of the
750 Carnmenellis Pluton. Journal of Petrology 27, 571–604.
751 Duchoslav, M., Marks, M.A.W., Drost, K., McCammon, C., Marschall, H.R., Wenzel, T., Markl, G.,
752 2017. Changes in tourmaline composition during magmatic and hydrothermal processes leading
753 to tin-ore deposition: The Cornubian Batholith, SW England. Ore Geology Reviews 83, 215–
754 234.
755 Duke, E.F., Papike, J.J., Laul, J.C., 1992. Geochemistry of a boron-rich peraluminous granite pluton: the
756 Calamity Peak layered granite-pegmatite complex, Black Hills, South Dakota. American
757 Mineralogist 30, 811–833.
758 Exley, C.S., Stone, M., 1982. Hercynian intrusive rocks. In: Sutherland, D.S. (ed) Igneous rocks of the
759 British Isles, Wiley, Chichester, 287‐320.
760 Floyd, P.A., Exley, C.S., Styles, M.T., 1993. Igneous Rocks of South-West England. Geological
761 Conservation Review Series, Chapman and Hall, London.
762 Förster, H.-J., Trumbull, R.B., Gottesmann, B., 1999. Late-collisional granites in the Variscan
763 Erzgebirge, Germany. Journal of Petrology 40, 1613–1645.
764 George, M.C., Stone, M., Fejer, E.E., Symes, R.F., 1981. Triplite from the Megiliggar Rocks, Cornwall.
765 Mineralogical Magazine 44, 236–238.
766 Gleeson, S.A., Wilkinson, J.J., Shaw, H.F., Herrington, R.J., 2000. Post‐magmatic hydrothermal
767 circulation and the origin of base metal mineralization, Cornwall, UK. Journal of the Geological
768 Society 157, 589–600.
769 Goad, B.E., Černý, P., 1981. Peraluminous pegmatitic granites and their pegmatite aureoles in the
770 Winnipeg River District, southeastern Manitoba. Canadian Mineralogist19, 177–194.

771 Goode, A.J.J., Taylor, R.T., 1988. Geology of the country around Penzance (Sheet 351/358). Memoir of
772 the British Geological Survey, HMSO, London.
773 Gottlieb, P., Wilkie, G., Sutherland, D., Ho-Tun, E., Suthers, S., Perera, K., Jenkins, B., Spencer, S.,
774 Butcher, A., Rayner, J., 2000. Using quantitative electron microscopy for process mineralogy
775 applications. JOM 52, 24–25.
776 Govindaraju, K., 1994. Compilation of working values and sample description for 383 geostandards.
777 Geostandards Newsletter 18, 1–158.
778 Hall, S., 1930. The geology of the Godolphin granite. A study of the coastal geology between
779 Perranuthnoe and Looe Pool. Proceedings of the Geologists´ Association 42, 117–147.
780 Hanchar, J.M., Hoskin, P.W.O., eds, 2003. Zircon. Reviews in Mineralogy and Geochemistry 53.
781 Henderson, C.M.B., Martin, J.S., Mason, R.A., 1989. Compositional relations in Li‐micas from SW
782 England and France: an ion‐ and electronmicroprobe study. Mineralogical Magazine 53, 427–
783 449.
784 Hosking, K.F.G., 1952. Cornish pegmatites and bodies with pegmatite affinities. Transaction Royal
785 geological Society of Cornwall 18, 411–455
786 Jacamon, F., Larsen, R.B., 2009. Trace element evolution of quartz in the charnockitic Kleivan granite,
787 SW Norway: the Ge/Ti ratio of quartz as an index of igneous differentiation. Lithos 107, 281–
788 291.
789 Jahns, R.H., Tuttle, O.F., 1963. Layered pegmatite-aplite intrusives. Mineralogical Society of America,
790 Special Papers 1, 78–92.
791 Johan, V., Johan, Z., 1994. Accessory minerals of the Cínovec (Zinnwald) granite cupola, Czech
792 Republic. Part 1: Nb-, Ta- and Ti-bearing oxides. Mineralogy and Petrology 51, 323–343.
793 Johannes, W., Holz, F., 1996. Petrogenesis and experimental petrology of granitic rocks. Minerals and
794 rocks 22, Springer, 335 pp.
795 Leveridge, B.E., Shail, R.K., 2011. The Gramscatho Basin, south Cornwall, UK: Devonian active
796 margin successions. Proceedings of the Geologists' Association 122, 568–615,

797 Linnen, R.L., 1998. The solubility of Nb-Ta-Zr-Hf-W in granitic melts with Li and Li+F: constraints for
798 mineralization in rare metal granites and pegmatites. Economic Geology 93, 1013–1025.
799 Linnen, R.L., Keppler, H., 1997. Columbite solubility in granitic melts: consequence for the enrichment
800 and fractionation of Nb and Ta in the Earth´s crust. Contributions to Mineralogy and Petrology
801 128, 213–227.
802 London, D., 2008. Pegmatites. Canadian Mineralogist Special Publication 10, 347 pp.
803 London, D., 2014. A petrologic assessment of internal zonation in granitic pegmatites. Lithos 184–187,
804 74–104.
805 London, D., 2015. Reply to Thomas and Davidson on "A petrologic assessment of internal zonation in
806 granitic pegmatites". Lithos 212–215, 469–484.
807 London, D., Manning, D.A.C., 1995. Chemical variation and significance of tourmaline from South
808 West England. Economic Geology 90, 495–519.
809 London, D., Morgan, VI G.B., Paul, K.A., Guttery, B.M., 2012. Internal evolution of miarolitic granitic
810 pegmatites at the Little Three mine, Ramona, California, USA. Canadian Mineralogist 50,
811 1025–1054.
812 Manning, D.A.C., 1981. The effect of fluorine on liquidus phase relationships in the system Qz-Ab-Or
813 with excess water at 1 kbar. Contribution to Mineralogy and Petrology 76, 206–215.
814 Manning, D.A.C., Exley, C.S., 1984. The origins of late-stage rocks in the St. Austell granite - a
815 reinterpretation. Journal of the Geological Society 141, 581–591.
816 Manning, D.A.C., Hill, P.I., 1990. The petrogenetic and metallogenetic significance of topaz granite
817 from the soutwest England orefield. Geological Society of America Special Paper 246, 51–69.
818 Manning, D.A.C., Hill, P.I., Howe, J.H., 1996. Primary lithological variation in the kaolinized St Austell
819 Granite, Cornwall, England. Journal of the Geological Society of London 153, 827–838.
820 Merlet, C., 1994. An Accurate Computer Correction Program for Quantitative Electron Probe
821 Microanalysis. Microchimica Acta 114/115, 363–376.
822 Müller, A., Williamson B.J., Smith M., 2005. Origin of quartz cores in tourmaline from Roche Rock,
823 SW England. Mineralogical Magazine 69, 381–401.

824 Müller, A., Seltmann, R., Halls, C., Siebel, W., Dulski, P., Jeffries, T., Spratt, J., Kronz, A., 2006. The
825 magmatic evolution of the Land´s End pluton, Cornwall, and associated pre-enrichment of
826 metals. Ore Geology Reviews 28, 329–367.
827 Müller, A., van den Kerkhof, A.M., Behr, H.-J., Kronz, A., Koch-Müller, M., 2010. The evolution of
828 late-Hercynian granites and rhyolites documented by quartz – a review. Geological Society of
829 America Special Papers 472, 185–204.
830 Neiva, A.M.R., Ramos, J.M.F., 2010. Geochemistry of granitic aplite-pegmatite sils and petrogenetic
831 links with granites, Guarda-Belmonte area, central Portugal. European Journal of Mineralogy
832 22, 837–854.
833 Norton, J.J., 1994. Structure and bulk composition of the Tin Mountain Pegmatite, Black Hills, South
834 Dakota. Economic Geology 89, 1167–1175.
835 Novák, M., Černý, P., Uher, P., 2003. Extreme variation and apparent reversal of Nb–Ta fractionation in
836 columbite-group minerals from the Scheibengraben beryl–columbite granitic pegmatite,
837 Maršíkov, Czech Republic. European Journal of Mineralogy 15, 565–574.
838 Pichavant, M., 1987. Effect of B and H_2O on liquidus phase relations in the haplogranite system at 1
839 kbar. American Mineralogist 72, 1056–1070.
840 Pownall, J.M., Waters, D.J., Searle, M.P., Shail, R.K., Robb, L.J., 2012. Shallow laccolithic
841 emplacement of the Land's End and Tregonning granites, Cornwall, UK: Evidence from aureole
842 field relations and P-T modelling of cordierite-anthophyllite hornfels. Geosphere 8, 1467–1504.
843 Raimbault, L., Cuney, M., Azencott, C., Duthou, J.L., Joron, J.L., 1995. Geochemical evidence for a
844 multistage magmatic genesis of Ta-Sn-Li mineralization in the granite at Beauvoir, French
845 Massif Central. Economic Geology 90, 548–596.
846 Reid, C., Flett, J.S. 1907. The geology of the Land's End District. Memoir of the British Geological
847 Survey, Sheets 351/358 (England and Wales).
848 Rusk, B.G., Lowers, H.A., Reed, M.H., 2008. Trace elements in hydrothermal quartzt: Relationship to
849 cathodoluminescent textures and insights into vein formation. Geology 36, 547–550.
850 Schaller, W.T., 1925. The genesis of lithium pegmatites. American Journal of Sciences 10, 269–279.

851 Shearer, C.K., Papike, J.J., Jollieff, B.L., 1992. Petrogenetic links among granites and pegmatites in the
852 Harney Peak rare-element granite-pegmatite system, Black Hills, South Dakota. Canadian
853 Mineralogist 30, 785–809.
854 Simmons, W. B., Heinrich, E. W., 1975. A summary of the petrogenesis of the granite-pegmatite system
855 in the northern end of the Pikes Peak batholith. Fortschritte der Mineralogie 52, 251–264.
856 Simons, B., Shail, R.K., Andersen, C.Q., 2016. The petrogenesis of the Early Permian granites of the
857 Cornubian batholith: lower plate post-collisional peraluminous magmatism in the
858 Rhenohercynian Zone of the SW England. Lithos 260, 76–94.
859 Simons, B.J., Andersen, J., Shail, R.K., Jenner, F.E., 2017. Fractionation of Li, Be, Ga, Nb, Ta, In, Sn,
860 Sb, W and Bi in the peraluminous Early Permian Variscan granites of the Cornubian Batholith:
861 precursor processes to magmatic-hydrothermal mineralisation. Lithos 278–281, 491–512.
862 Stepanov, A.S., Hermann, J., 2013. Fractionation of Nb and Ta by biotite and phengite: Implications for
863 the "missing Nb paradox". Geology 41, 303–306.
864 Stone, M., 1960. The Tregonning-Godolphin granite. In: Robson, J. and Simpson, S. (eds) Proceedings
865 of the Conference of Geologists and Geomorphologists working in South West England. Pp. 14–
866 16. Bristol.
867 Stone, M., 1966. Fold structures in the Mylor Beds, near Porthleven, Cornwall. Geological Magazine
868 103, 440–60.
869 Stone, M., 1969. Nature and origin of banding in the granitic sheets Tremarne, Porthleven, Cornwall.
870 Geological Magazine 106, 142–158.
871 Stone, M., 1975. Structure and petrology of the Tregonning-Godolphin granite, Cornwall. Proceedings
872 of the Geologists' Association 86, 155–170.
873 Stone, M. 1992. The Tregonning granite: petrogenesis of Li-mica granites in the Cornubian batholith.
874 Mineralogical Magazine 56, 141–155.
875 Stone, M., Awad, N.T.I., 1988. behaviour of trace-alkali and other elements at Tregonning granite –
876 pelite contacts. Proceedings of the Ussher Society 7, 47–51.

877 Stone, M. Exley, C.S., 1985. High heat production granites of southwest England and their associated
878 mineralization: a review. In: High Heat Production (HHP) granites, hydrothermal circulation
879 and ore genesis, 571–593.
880 Stone, M., Exley, C.S., George, M.C., 1988. Compositions of trioctahedral micas in the Cornubian
881 batholith. Mineralogical Magazine 52, 175–192.
882 Stone, M., George, M.C., 1978. Amblygonite in the leucogranites of the Tregonning-Godolphin granite,
883 Cornwall. Mineralogical Magazine 42, 151–152.
884 Swanson, S.E., 1977. Relation of nucleation and crystal-growth to the development of granitic textures.
885 American Mineralogist 62, 966–978.
886 Thomas, R., Webster, J.D., Rhede, D., Seifert, W., Rickers, K., Förster, H.-J., Heinrich, W., Davidson,
887 P., 2006. The transition from peraluminous to peralkaline granitic melts: evidence from melt
888 inclusions and accessory minerals. Lithos 91, 137–149.
889 Thomas, R., Davidson, P., 2012. Water in granite and pegmatite-forming melts. Ore Geology Reviews
890 46, 32–46.
891 Thomas, R., Davidson, P., 2013. The missing link between granites and granitic pegmatites. Journal of
892 Geosciences 58, 183–200.
893 Thomas, R., Davidson, P., 2015. Comment on "A petrologic assessment of internal zonation in granitic
894 pegmatites" by David London (2014). Lithos 212–215, 462–468.
895 Van Lichtervelde, M., Linnen, R., Salvi, S., Beziat, D., 2006. The role of metagabbro rafts on tantalum
896 mineralization in the Tanco granitic pegmatite, Manitoba. Canadian Mineralogist 44, 625–644.
897 Webber, K.L., Falster, A.U., Simmons, W.B., Foord, E.E., 1997. The role of diffusion-controlled
898 oscillatory nucleation on the formation of line rock in pegmatite-aplite dikes. Journal of
899 Petrology 38, 1777–1791.
900 Webber, K.L., Simmons, W.B., Falster, A.U., Foord E.E., 1999. Cooling rates and crystallization
901 dynamics of shallow level pegmatite-aplite dikes, San Diego County, California. American
902 Mineralogist 84, 708–717.
903 Wilkinson, J.J., 1990. The role of metamorphic fluids in the development of the Cornubian ore field:
904 fluid inclusion evidence from south Cornwall. Mineralogical Magazine 54, 219–230.

Wilkinson, J.J., 1991. Volatile production during contact metamorphism: the role of organic matter in pelites. Journal of the Geological Society London 148, 731–736.

Willis-Richards, J., Jackson, N.J., 1989. Evolution of the Cornubian ore field, southwest England: Part 1. Batholith modelling and ore distribution. Economic Geology 84, 1078–1100.

Wise, M.A., Francis, C.A., Černý, P., 2012. Compositional and structural variations in columbite-group minerals from granitic pegmatites of the Brunswick and Oxford fields, Maine: differential trends in F-poor and F-rich environments. Canadian Mineralogist 50, 1515–1530.

Tables

Table 1 Chemical composition of studied rocks (major elements in wt.%, trace elements in ppm)

Tables only as electronic appendices:

Supplementary table 1 Modal (vol.%) and computed chemical (wt.%) composition of layered portion of a complex sheet (sample#2015)

Supplementary table 2 Modal (vol.%) and computed chemical (wt.%) composition of layered portion of an aplite-pegmatite sheet (sample#4965)

Supplementary table 3 Trace element concentrations in quartz (ppm) by LA-ICP-MS

Supplementary table 4 Chemical composition (wt.%, by EMPA) and empirical formulae of feldspars

Supplementary table 5 Chemical composition (wt.%, by EMPA) and empirical formulae of mica

Supplementary table 6 Trace element contents in mica (ppm) by LA-ICP-MS

Supplementary table 7 Chemical composition (wt.%, by EMPA) and empirical formulae of tourmaline

Supplementary table 8 Trace element contents in tourmaline (ppm) by LA-ICP-MS

Supplementary table 9 Chemical composition (wt.%, by EMPA) and empirical formulae of Ti, Sn, W, Nb, Ta minerals

Supplementary table 10 Chemical composition (wt.%, by EMPA) and empirical formulae of zircon

Supplementary table 11 Detection limits of trace elements in the whole-rock analyses (ppm)

Explanation to figures

Fig. 1 A- Geological sketch map of granite plutons in Cornwall (acc. to Simons et al., 2016); B-Schematic section through Megiliggar Rocks showing the location of samples (not to scale). The total length of the section is ca. 600 m. The sheets are likely to represent apophyses of residual melt which escaped from the largely crystallized roof of the granite pluton. With increasing distance from the Tregonning Granite, the silicate melt crystallized as homogeneous leucogranite sheets, banded complex sheets (i.e. combinations bands with granitic, aplitic and pegmatitic textures), and layered aplite-pegmatites. A gradual change in textures away from the granite margin, together with similarities in whole-rock chemical compositions, provide strong evidence for a genetic link between the Tregonning Granite and Megiliggar Sheet Complex.

Fig. 2 Field photographs: **a**, cliff at Megiliggar Rocks, western part of the major leucogranite sheets (up to 2.5 m thick) laterally (to the right) passing into "complex sheets"; **b**-**e**, the textural evolution of the sheets with increasing distance from the Tregonning Granite (from West to East):
Close to the granite the sheets are more or less homogeneous (leucocratic sheet granite). About 50 m from the contact the first layered structures can be traced caused by a local enrichment in mica (b). Further on (c. 75 m) grain-size differences between individual layers start to develop, in addition to the local mica enrichments, and about 100 m away the first thin veinlets with pegmatitic textures appear within the sheet (c). Further east the borders between the layers become more distinct; the differences in the grain sizes of the aplitic, granitic and pegmatitic layers increases together with the thickness in particular of the pegmatitic layers (d to e)." **f,** bifurcation of a thin (~30 cm) aplite-pegmatite sheet, showing comb K-feldspar crystals along both the contact in the upper sheet vs. central position in the lower sheet; **g**. steeply inclined, thin (~10–15 cm) aplite-pegmatite sheet cutting the slate in the eastern part of the cliff.

Fig. 3 Rock textures: **a**, Tregonning granite (#5303); **b**, typical layering in the "complex sheets" composed of granitic (G), pegmatitic (P) and aplitic (A) layers (#5305); **c**, aplite-pegmatite sheet with aplitic layer near the contact and coarse-grained granite to pegmatite in the centre (# 5306 resp.

#5307); **d**, aplite-pegmatite sheet with pegmatitic (stockscheider-like) rim and aplitic centre. Contact plane between the sheets and Mylor Slates is highlighted by arrows.

Fig. 4 Detailed investigation of a finely-banded portion of a complex sheet (sample 2015): left - photo of an 18 cm wide cut sample face; Central - mineral map determined by TIMA (in the middle, Kfs (K-feldspar)- red, Ab (Albite) – light blue, Qtz (Quartz) – dark blue, Msc (Muscovite) – pink, Zin (Zinnwaldite) –brown, Tur (Tourmaline) – green), Rest – other accessory minerals; Right - mineral composition of individual bands (vol.%). Crystallization of the rock proceeded upwards.

Fig. 5 Detail investigation of a tourmaline aplite (sample 4965): left - photo of a 12.5 cm wide sample cut face; middle - mineral map determined by TIMA (Kfs (K-feldspar) – red, Ab (Albite) – light blue, Qtz (Quartz) – dark blue, Msc (Muscovite) – pink, Tur (Tourmaline) – dark green, Toz (Topaz) – black, Ap (Apatite) – yellow-green), Rest – other accessory minerals; Right - mineral composition of individual bands (vol.%). The crystallization proceeded upwards.

Fig. 6 Approximate chemical composition of individual layers in finely banded rocks computed from modal compositions and chemical analyses of minerals: **a**, distribution of selected elements across the layering (#2015); **b**, K_2O vs. Na_2O; **c**, B_2O_3 vs. F; **d**, FeO vs. B. Mean values of the whole samples are highlighted by red marks in diagrams b–d.

Fig. 7 Whole-rock compositions of studied rocks. In diagram f, only typical analyses are shown. Note the tetrad effect in Fig. e! Contents of some of the REE in the sheet leucogranite are below the detection limits of ICP-MS.

Fig. 8 Trace elements in quartz: **a**, Al vs. Ti; **b**, Al/Ti vs. Li; **c**, Al/Ti vs. Ge. Data from Variscan granites (I-, S-, A-types, Breiter et al. 2013) and pegmatites (muscovite to lepidolite types, Breiter et al. 2014) from the Bohemian Massif are shown for comparison.

990 **Fig. 9** Chemical composition of micas: **a**, Si vs. Fe; **b**, Si vs. F; **c,** composition of micas (means of 4–5
991 EMPA analyses) across the finely banded portion of a complex sheet (sample#2015); d, Li vs. Ta; e,
992 Li vs. Nb. In diagrams a–b, three groups of micas are highlighted: I, zinnwaldite–trilithionite series; II,
993 muscovite–phengite series; III, altered (?) Li-Fe-Al mica.
994
995 **Fig. 10** Chemical composition of tourmaline: **a**, Fe/(Mg+Fe) vs. □/(□+Na+K) (apfu); **b**, F vs.
996 □/(□+Na+K) (apfu); **c**, occupation of the Y-site (apfu); **d**, Li vs. Sn (ppm).
997
998 **Fig. 11** BSE-images of minerals: **a**, Nb-Ta-rich rutile (grey) with inclusions of W-rich Fe-columbite
999 (bright), #2015, in banded rock; **b**, patchy zoned Nb-Ta-enriched rutile (grey) with small crystals of
1000 tantalite (bright), #5303, in Tregonning granite; **c**, rutile with inclusions of columbite and ixiolite,
1001 #4964, in composite granite/pegmatite sheet; **d**, intergrowth of cassiterite (bright) and rutile (dark
1002 grey), #5304, in granitic part of the composite granite/pegmatite sheet; **e**, needle-like crystals of Mn-
1003 columbite with Ta-enriched rims in Li-mica, #4963, in leucocratic sheet granite; **f**, crystals of Fe-
1004 columbite (light grey with bright zones) in association with two colander-like zircon crystals, #5302,
1005 in coarse grained tourmaline-bearing sheet granite; **g**, monazite (Mnz) associated with xenotime (Xen),
1006 zircon (Zrn), Mn-rich apatite (Ap), pyrite (Py) and tourmaline (Tur) in quartz, #2015, in banded rock;
1007 **h**, crystal of uraninite (bright) rimmed by pyrite in quartz, #2015, in banded rock; **i**, grain of uraninite
1008 (bright) with thin rim of pyrite associated with a Nb, Y-phase, #5307, in pegmatitic core of composite
1009 aplite/pegmatite sheet; **j**, central part of an altered zircon grain contains numerous inclusions of
1010 uraninite while its rim is inclusions free, #4965, in tourmaline-rich banded rock; **k**, zoned zircon with
1011 Hf-enriched rim, in leucocratic sheet granite, #4963; **l**, zoned crystal of arsenopyrite, #2015, in banded
1012 rock. White scale bars in all cases 50μm.
1013
1014 **Fig. 12** Nb-Ta-Sn-W-oxide cross plots: **a**, Nb vs. Ta in rutile; **b**, columbite classification diagram; **c**,
1015 W vs. Mn/(Fe+Mn) in columbite and "ixiolite". Coloured symbols = columbite, empty symbols =
1016 ixiolite.
1017

Fig. 13 Relation between the Zr/Hf ratios and U concentrations in zircon (using data also from Breiter et al., 2016).

Fig. 14 Variation in the Nb/Ta ratio at Megiliggar Rocks: **a**, Nb/Ta vs. F in whole rocks; **b**, Nb/Ta vs. Li_2O in whole rocks; **c**, Nb vs. Ta in micas; **d**, Li vs. Nb/Ta in micas; **e**, Nb vs. Ta in tourmaline; **f**, Li vs. Nb/Ta in tourmaline.

Fig. 15a Composition of whole rocks and individual bands in banded rocks in the Qtz-Ab-Kfs triangle. Note systematic evolution of the lower (older) part of the sample #2015: systematic shift to the Ab-apex from line 1 to 7 (red arrow). Later zones, poorer in Kfs, scatter along the Qtz-Ab join. Sample #4965 represents the aplite-pegmatite melt with rather chaotic zoning; **b** Composition of proposed starting melt (Tregonning granite) and the Megiliggar sheet rocks computed according to whole-rock chemical data and EMPA of rock-forming minerals (sample 2015 acc. to modal analyse by TIMA). Three typical compositions of the George Ashley pegmatite (layered aplite rich in Ab, whole dyke, granular pegmatite rich in Kfs) acc. to Webber et al. (1997) and water-saturated leucogranitic solidus with 1 wt.% added F, resp. B (Manning, 1981 resp. Pichavant, 1987) are also shown for comparison.

Additional rock and mineral images in electronic form are available as a "Supplementary image pdf-file"

Figure 1

Click here to download high resolution image

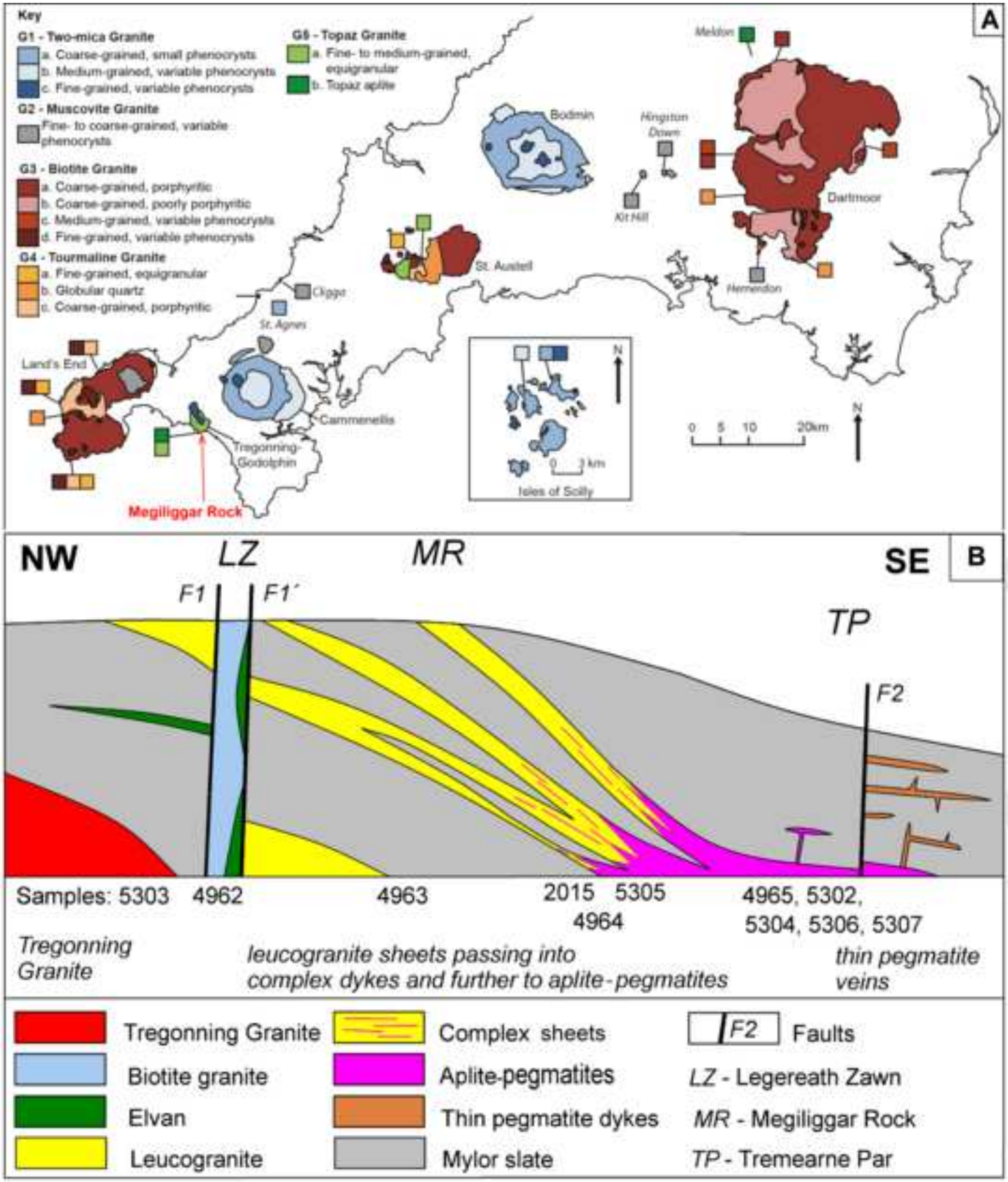

Figure 2

Click here to download high resolution image

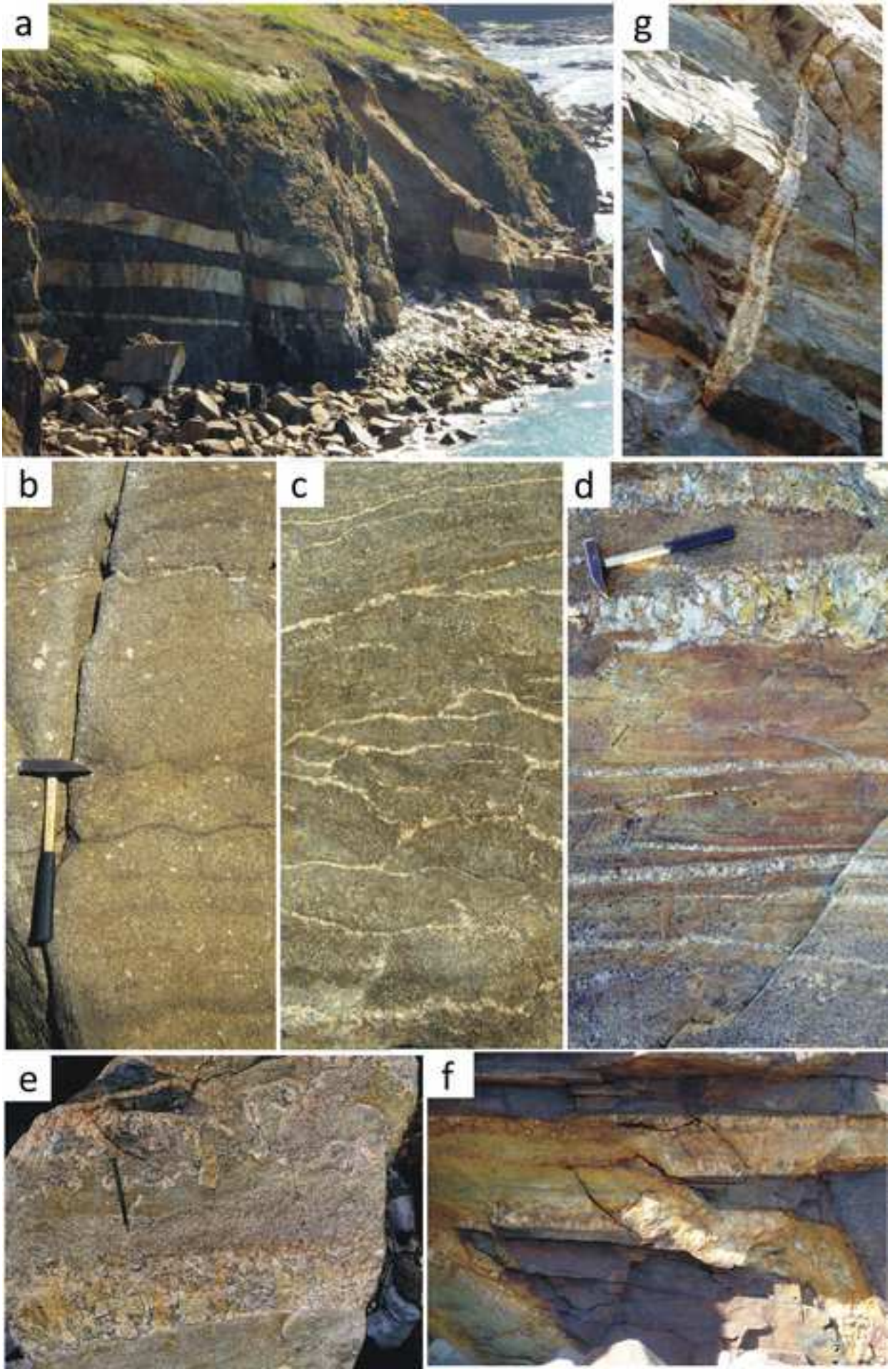

Figure 3

Click here to download high resolution image

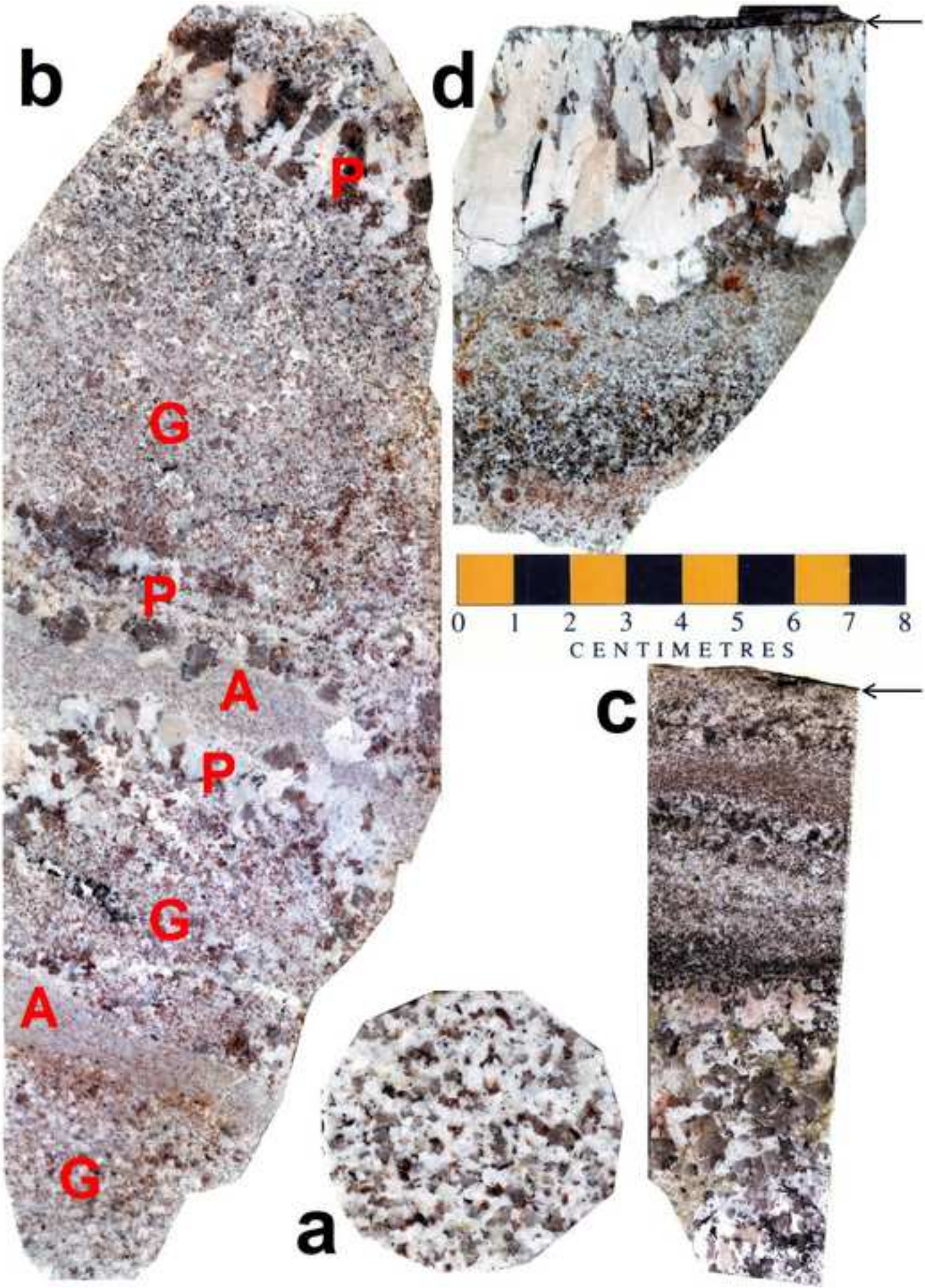

Figure 4

Click here to download high resolution image

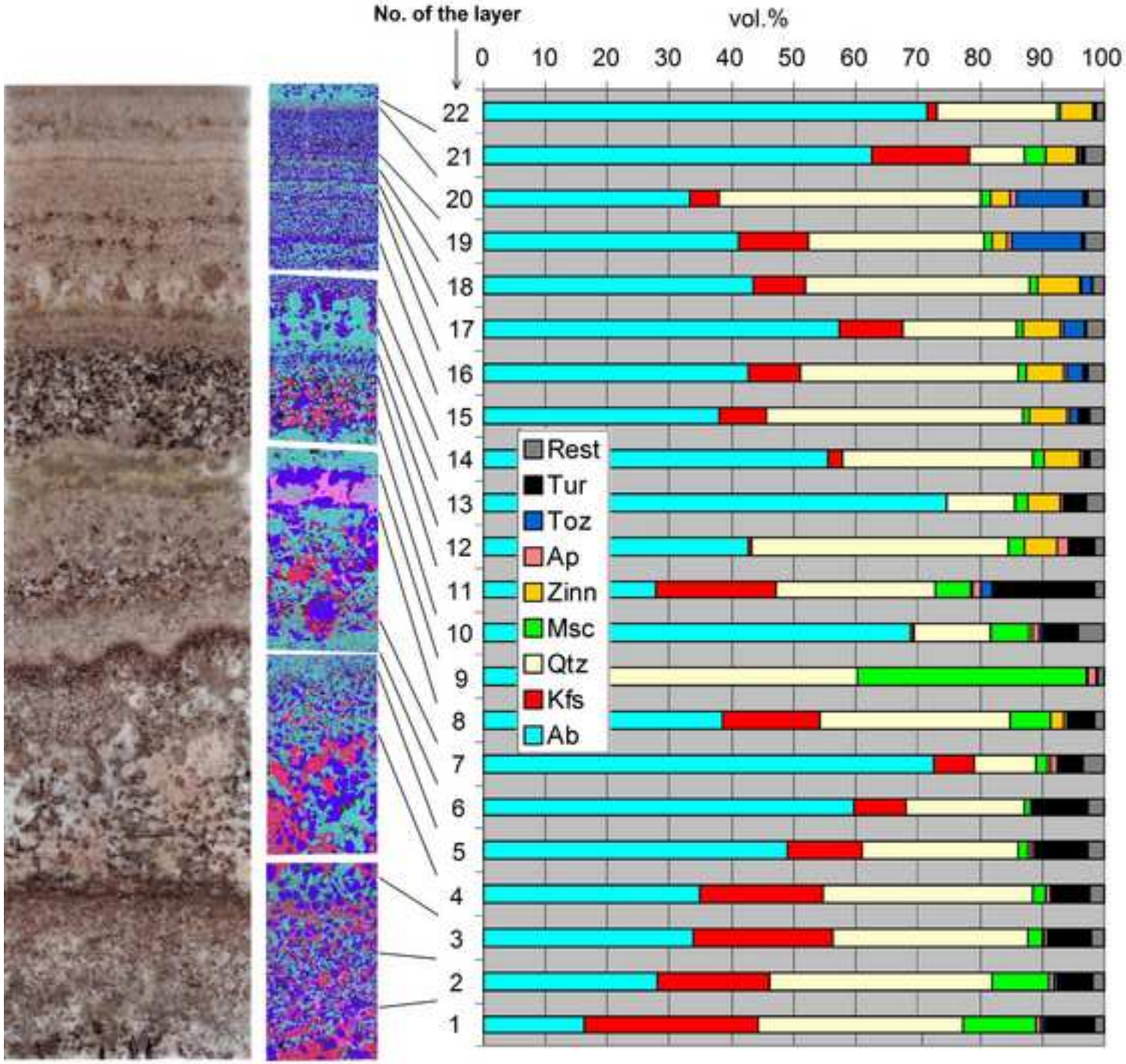

Figure 5

Click here to download high resolution image

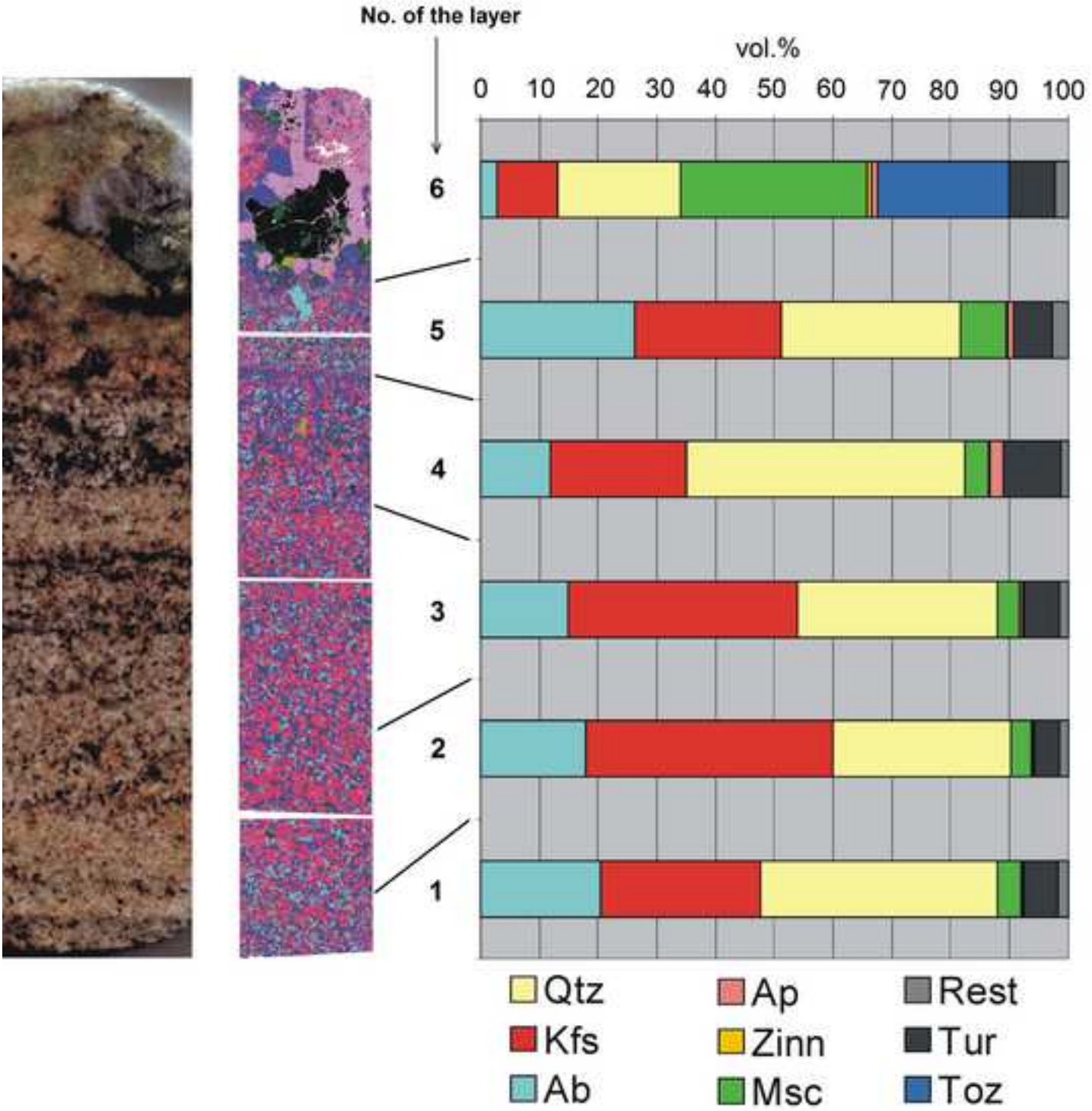

Figure 6

Click here to download high resolution image

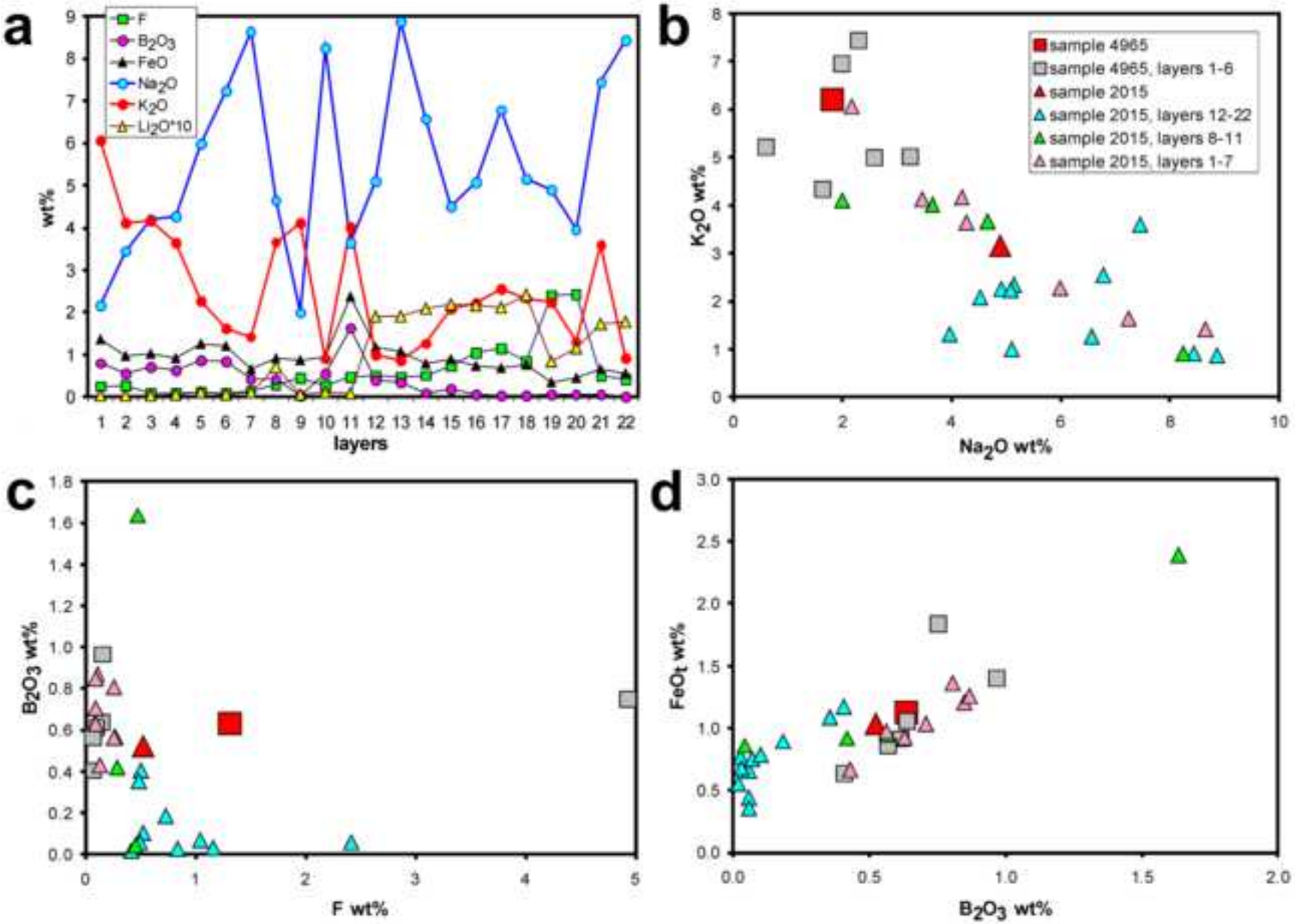

Figure 7

Click here to download high resolution image

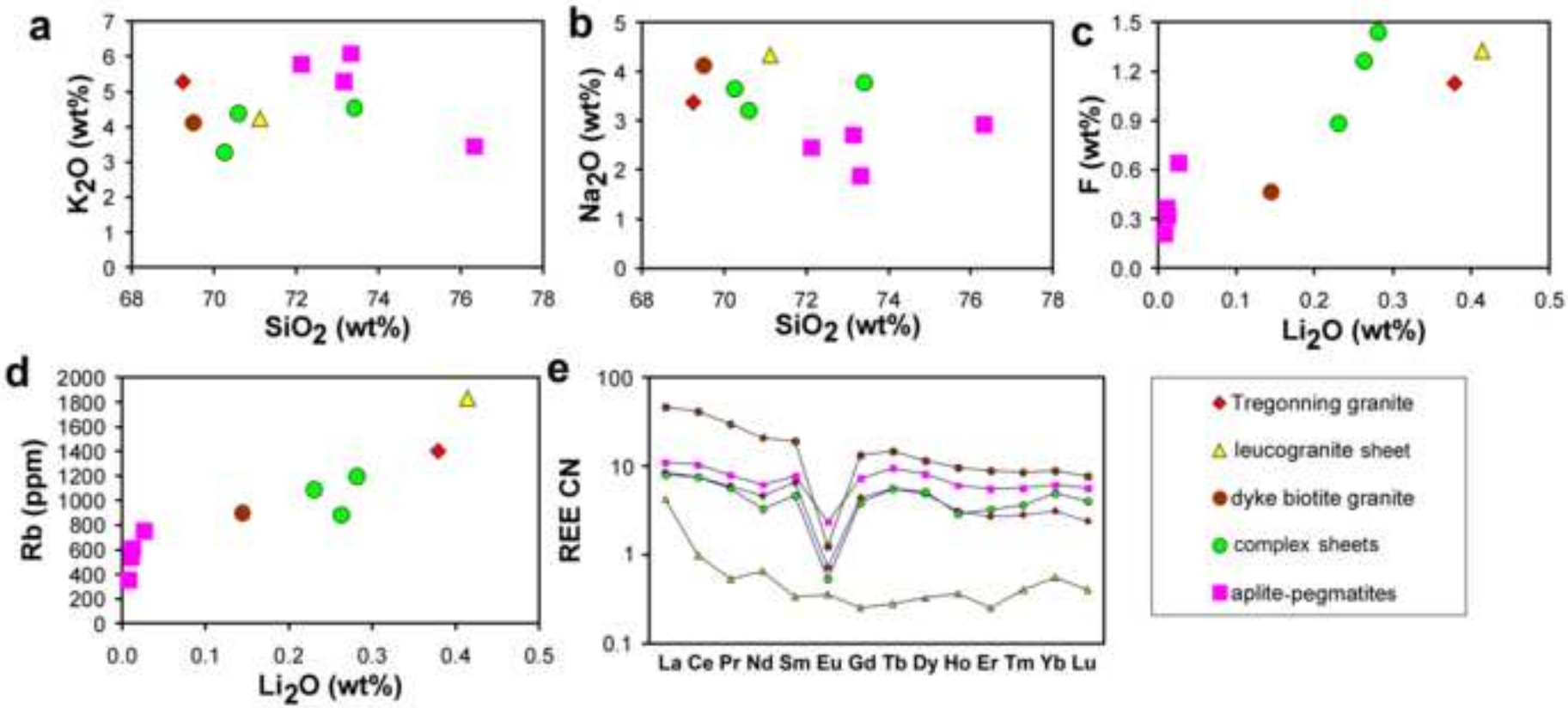

Figure 8

Click here to download high resolution image

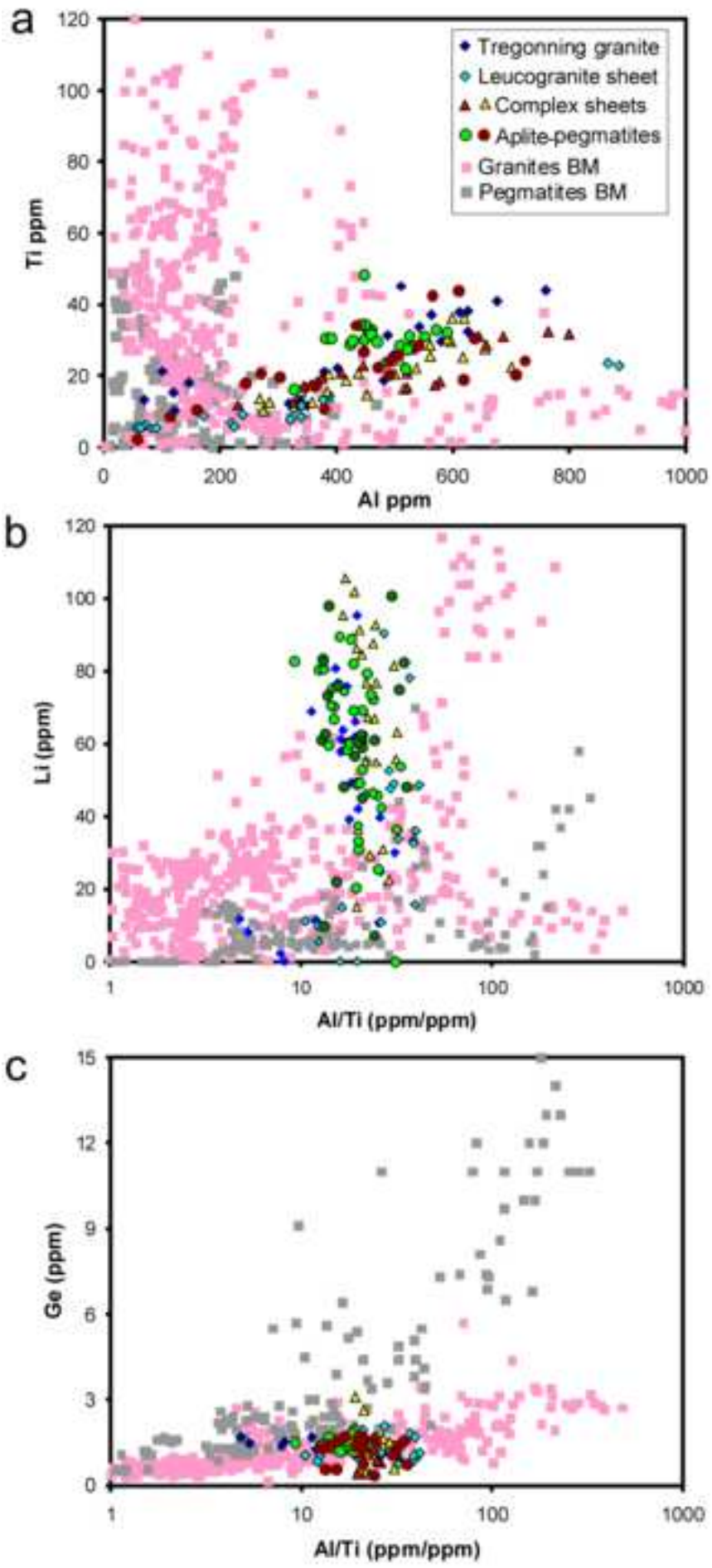

Figure 9

Click here to download high resolution image

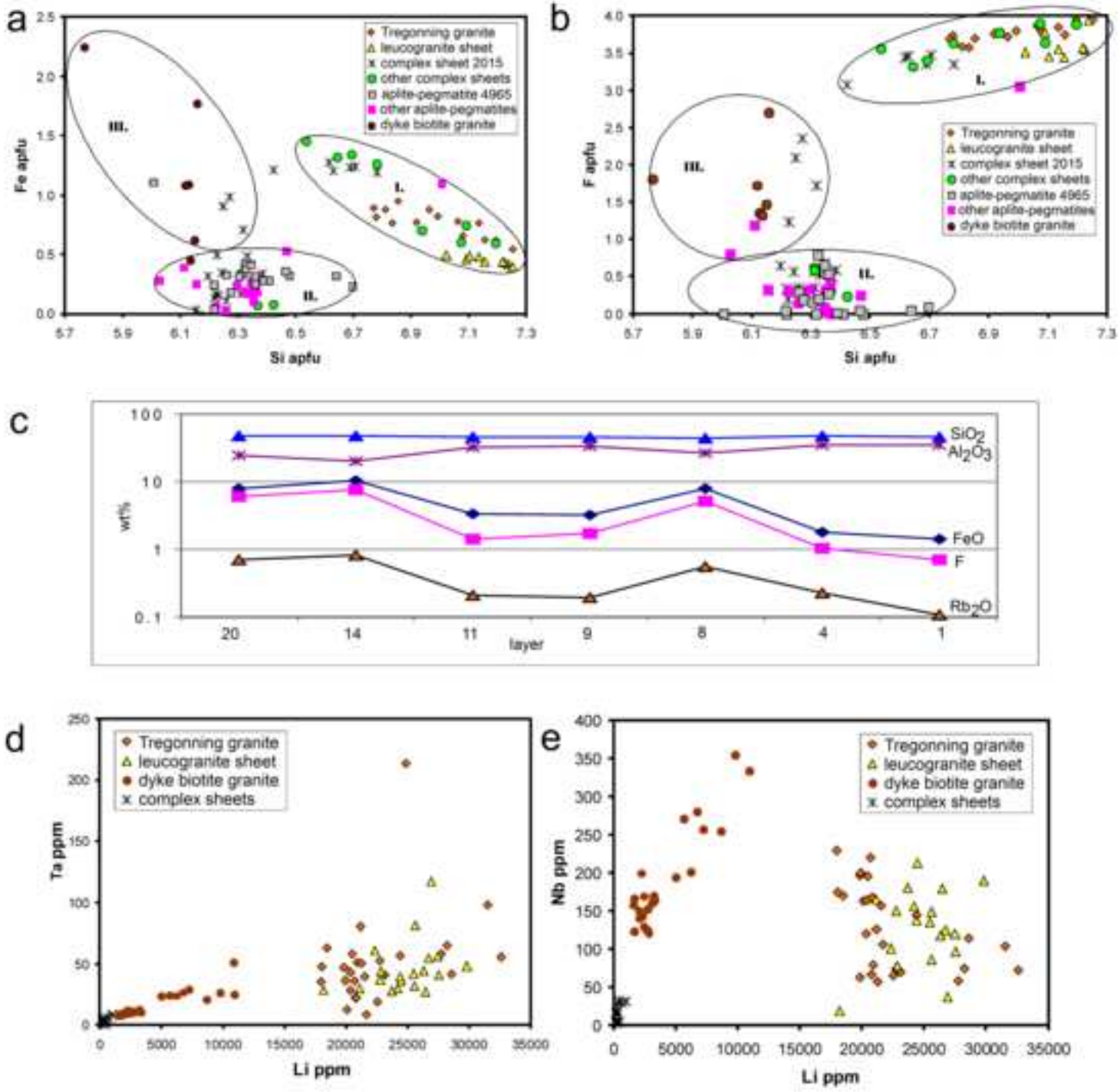

Figure 10

Click here to download high resolution image

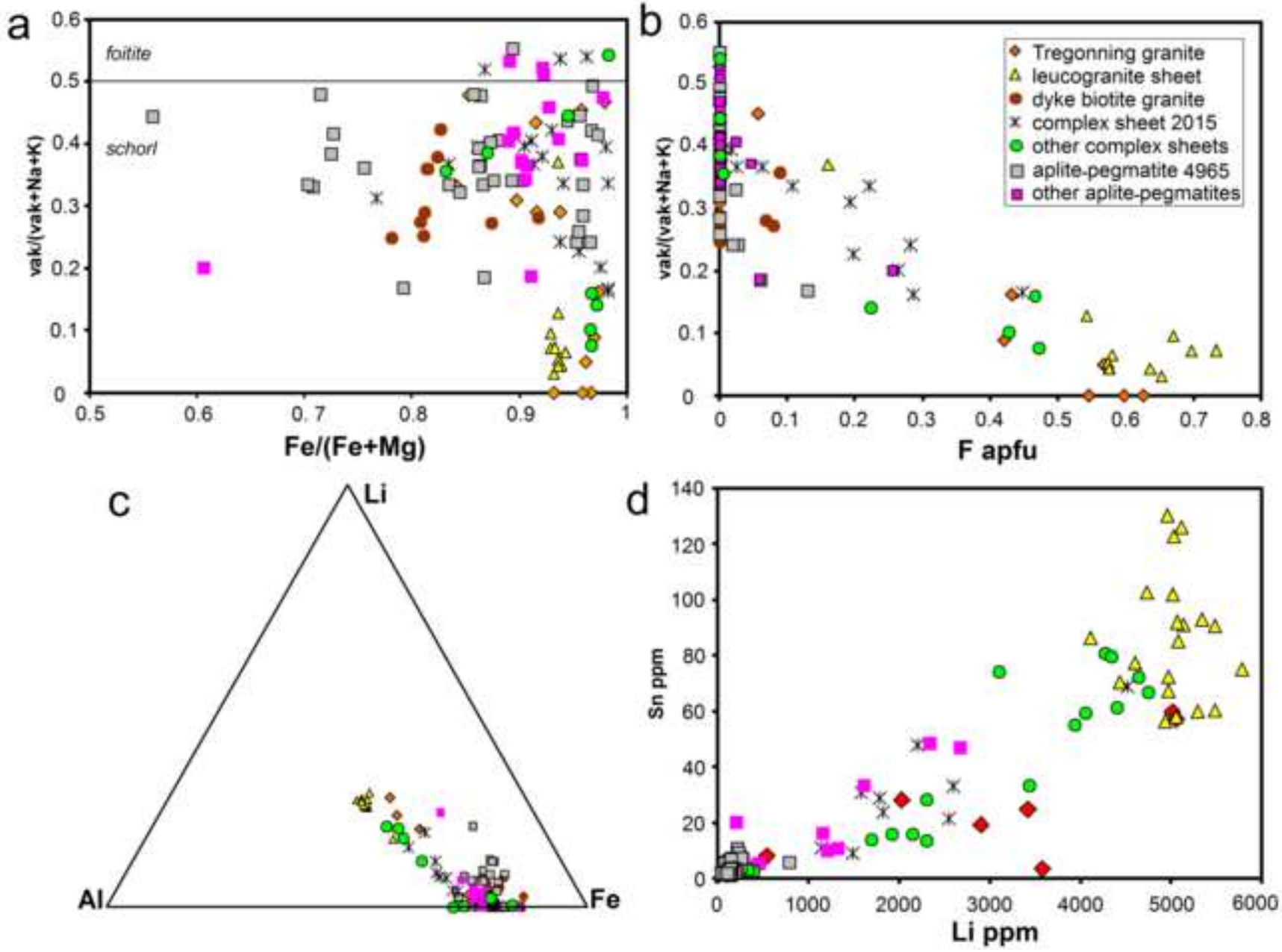

Figure 11

Click here to download high resolution image

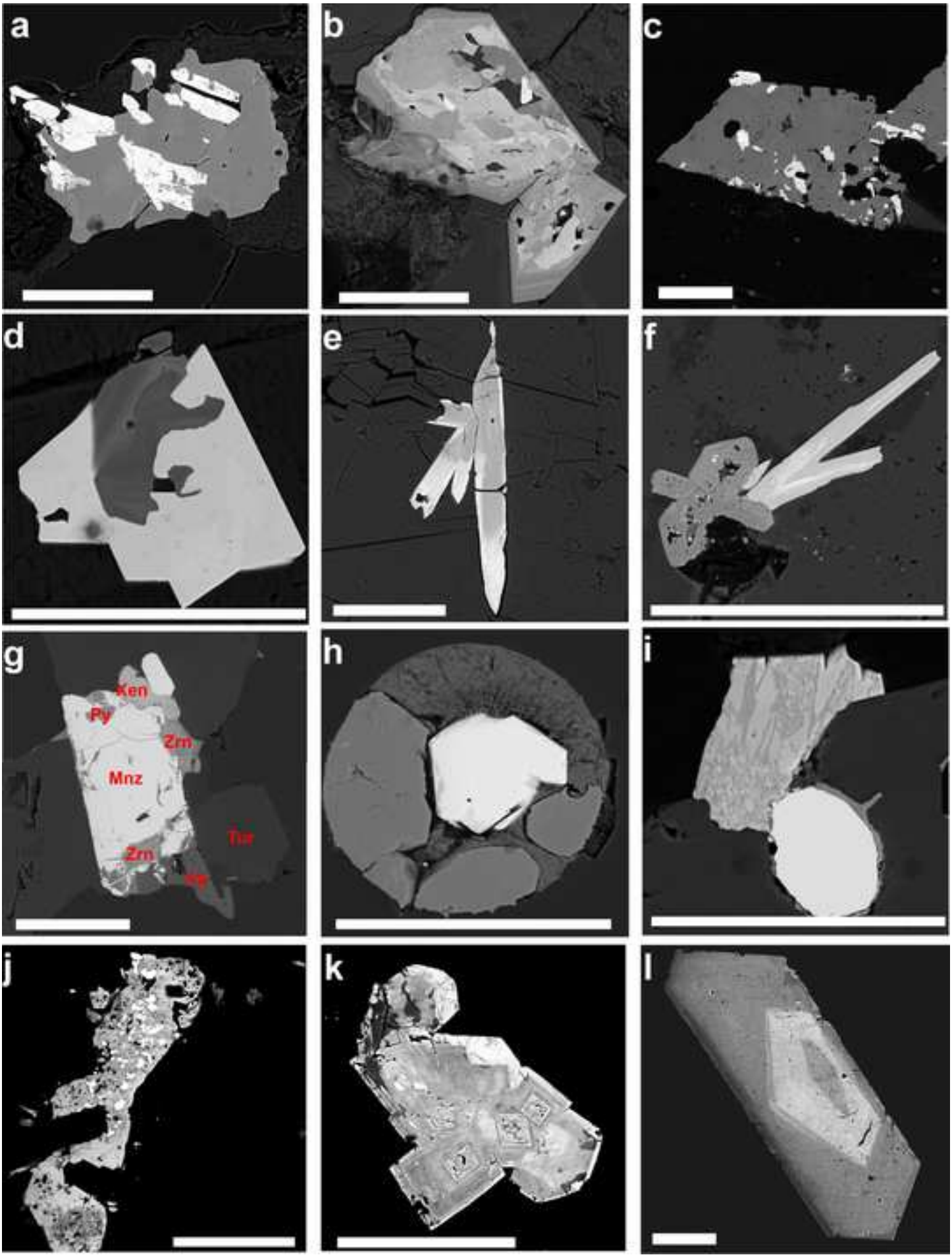

Figure 12

Click here to download high resolution image

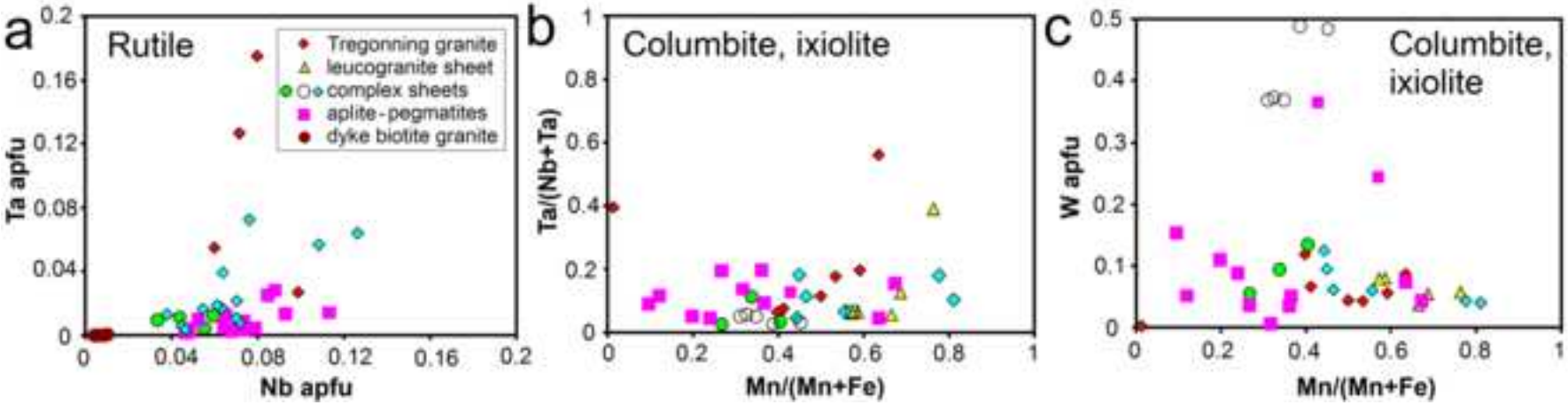

Figure 13

Click here to download high resolution image

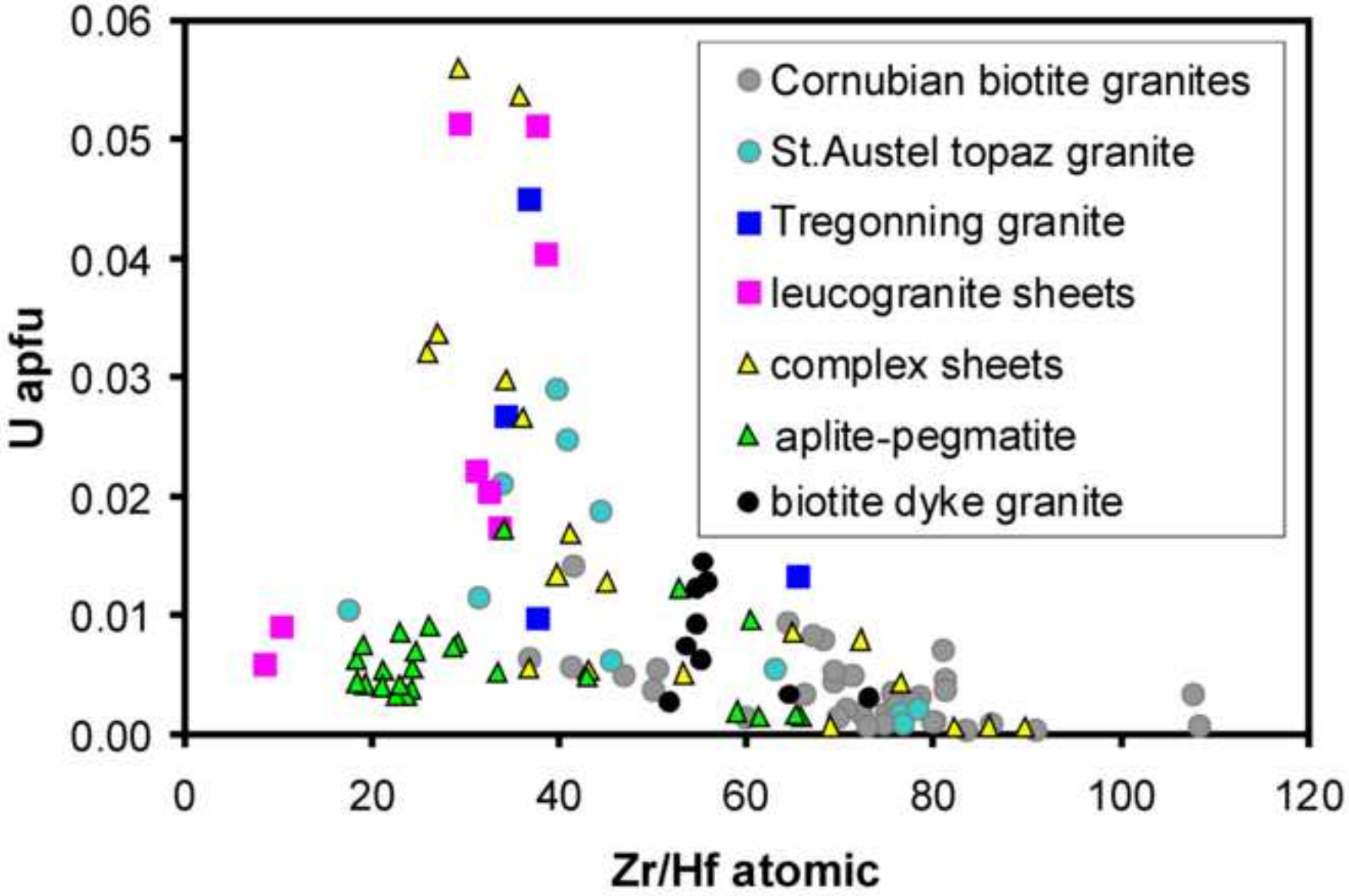

Figure 14

Click here to download high resolution image

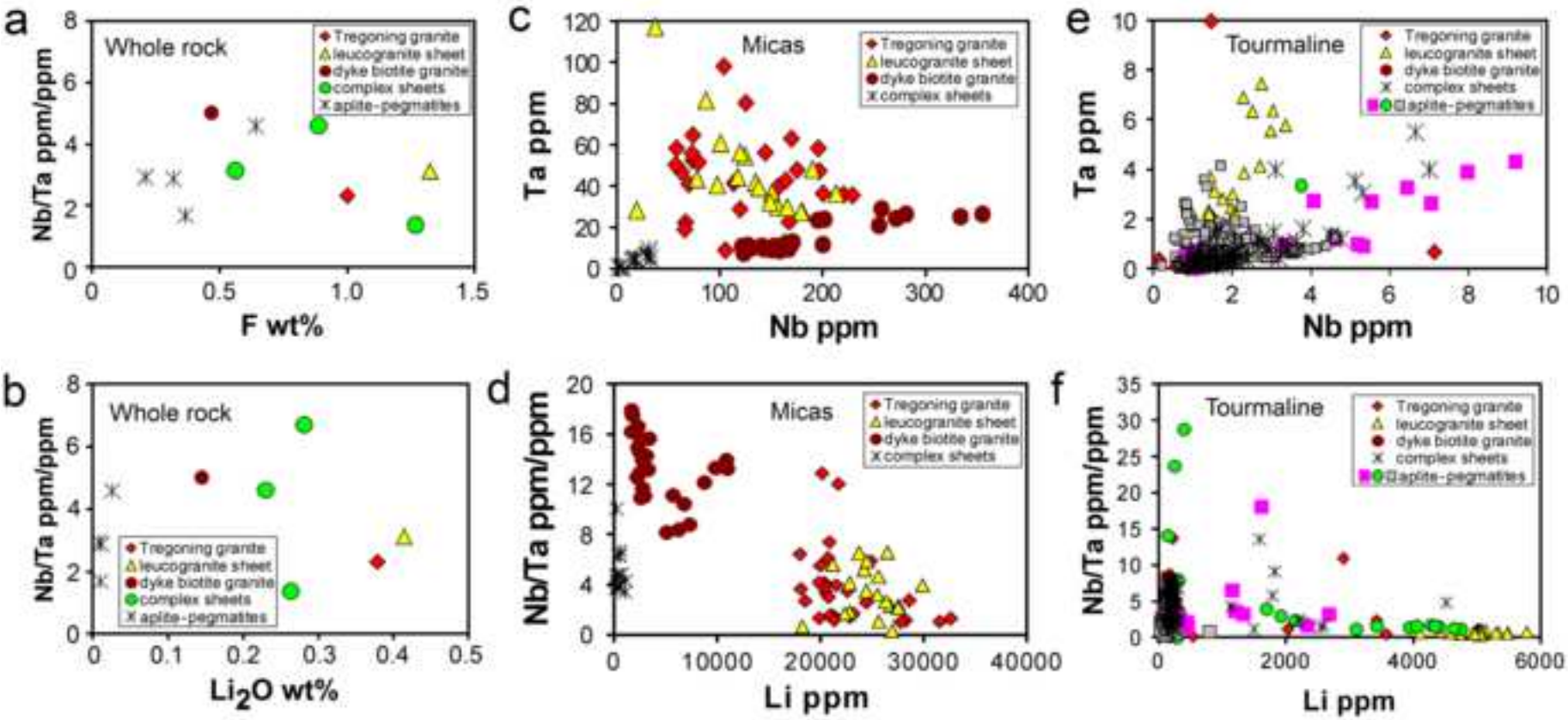

Figure 15

Click here to download high resolution image

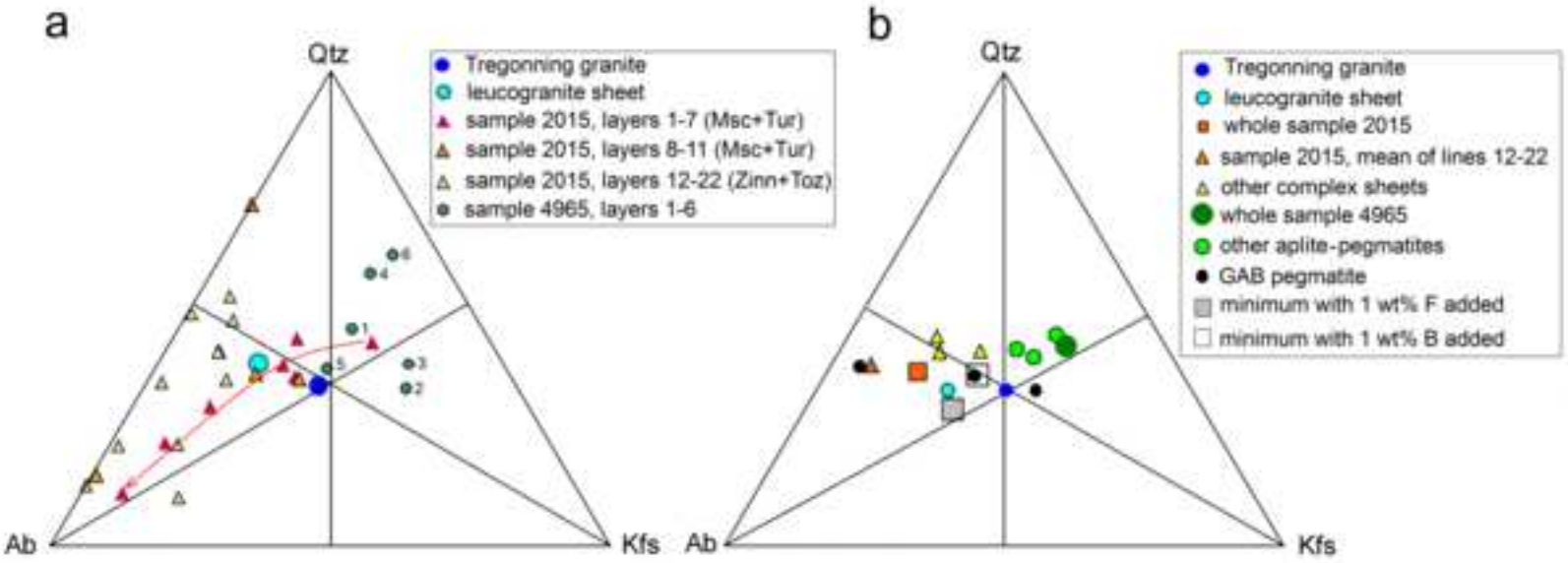

Table 1

Click here to download Table: Table 1 Chemical composition of studied rocks new.doc

Table 1 Chemical composition of studied rocks (wt.%, trace elements in ppm)

	Granites				Complex sheets (Li-mica bearing)				Aplite-pegmatites (tourmaline dominated)			
											Layered sheet	
	Tregoning Granite	Leuco-granite sheet	Biotite granite dyke		Layered granite-pegmatite	Fine grained aplite	Layered granite-pegmatite		Granite-pegmatite	Layered aplite	Aplite margin	Pegmatite core
Sample	**5303**	**4963**	**4962**		**4964**	**5304**	**5305**		**5302**	**4965**	**5306**	**5307**
SiO_2	69.23	71.11	69.49		70.58	70.25	73.40		73.14	73.31	72.11	76.31
TiO_2	0.05	0.01	0.10		0.04	0.10	0.11		0.04	0.03	0.02	0.03
Al_2O_3	16.66	15.57	16.84		15.52	15.18	14.03		15.09	14.36	16.30	13.75
Fe_2O_3	0.28	0.14	0.55		0.21	0.56	0.25		0.54	0.50	0.45	0.67
FeO	0.58	0.37	0.87		1.04	0.33	0.63		0.14	0.25	0.18	0.20
FeOtot	0.83	0.50	1.37		1.23	0.84	0.85		0.63	0.70	0.58	0.80
MgO	0.12	0.07	0.26		0.09	0.19	0.07		0.08	0.21	0.14	0.19
MnO	0.04	0.09	0.05		0.07	0.06	0.04		0.01	0.02	0.01	0.03
CaO	0.39	0.23	0.54		0.61	1.54	0.44		0.40	0.55	0.60	0.48
Li_2O	0.38	0.41	0.14		0.28	0.26	0.23		0.03	0.01	0.01	0.01
Na_2O	3.37	4.33	3.83		3.21	3.66	3.78		2.71	1.88	2.46	2.93
K_2O	5.28	4.23	4.13		4.39	3.28	4.54		5.30	6.09	5.79	3.45
P_2O_5	0.41	0.52	0.31		0.48	0.77	0.45		0.38	0.33	0.42	0.31
F	1.13	1.33	0.47		1.44	1.27	0.89		0.64	0.37	0.32	0.21
L.O.I.	1.20	1.00	1.37		1.27	1.60	0.96		0.76	0.91	0.84	0.84
$H_2O(-)$	0.11	0.16	0.37		0.22	0.15	0.09		0.07	0.40	0.08	0.12
F(ekv)	-0.47	-0.56	-0.20		-0.61	-0.53	-0.37		-0.27	-0.15	-0.13	-0.09
Total	99.23	99.56	99.32		99.46	99.20	99.90		99.33	99.21	99.73	99.52
Ba	12	5	25		11	35	19		16	128	63	45
Be	7	9	9		4	10	2		1	10	4	<1
Cs	199	253	74		107	182	88		33	23	25	17
Ga	42	45	39		44	48	43		40	24	33	29
Hf	1.1	1.1	2.7		0.8	1.6	0.9		0.7	1.6	1.4	0.9
Nb	40	52	33		68	69	57		38	34	26	17
Rb	1401	1832	898		1201	885	1091		755	538	613	356
Sn	22	80	26		17	61	13		13	14	15	13
Sr	24	17	20		11	116	17		11	59	40	27
Ta	17.3	16.7	6.6		10.1	50	12.4		8.2	20.4	9.1	5.8
Th	1	1	7		1	1	1		1	2	2	1
U	16	9	39		6	21	7		3	16	25	14
V	<8	<8	9		<8	14	9		<8	<8	<8	<8
W	30	37	19		28	46	21		10	4	5	8
Zr	17	13	62		9	23	12		11	26	29	15
Y	5.6	0.6	14.4		7.7	5.0	5.0		4.2	4.4	11.4	7.5
La	2.0	1.0	11.0		1.9	1.9	1.7		1.2	2.5	2.6	1.7
Ce	4.6	0.6	25.0		4.6	3.7	3.0		3.2	5.7	6.3	4.2
Pr	0.6	0.1	2.7		0.5	0.4	0.5		0.4	0.6	0.7	0.5
Nd	2.1	<0.3	9.5		1.5	1.6	1.7		1.4	2.2	2.8	1.8
Sm	1.0	<0.05	2.8		0.7	0.7	0.7		0.6	0.8	1.1	0.8
Eu	0.04	<0.02	0.07		0.03	0.06	0.04		0.04	0.19	0.13	0.12

Gd	0.87	<0.05	2.63		0.76	0.71	0.70		0.74	0.72	1.44	1.07
Tb	0.20	0.01	0.53		0.20	0.15	0.16		0.15	0.14	0.34	0.24
Dy	1.19	0.08	2.82		1.25	0.83	0.89		0.85	0.82	1.99	1.42
Ho	0.17	<0.02	0.53		0.16	0.13	0.12		0.12	0.15	0.33	0.19
Er	0.43	0.04	1.41		0.52	0.33	0.33		0.31	0.47	0.88	0.60
Tm	0.07	0.01	0.21		0.09	0.06	0.05		0.05	0.07	0.14	0.09
Yb	0.50	0.09	1.41		0.79	0.40	0.49		0.42	0.51	0.98	0.60
Lu	0.06	0.01	0.19		0.10	0.07	0.05		0.06	0.06	0.14	0.09
Mo	0.3	<0.1	0.3		<0.1	2.3	<0.1		<0.1	1.0	1.9	1.7
Cu	1.9	0.8	2.8		1.3	0.8	0.8		1.0	1.6	0.6	1.2
Pb	10	7	13		5	6	7		12	19	13	7
Zn	41	35	61		47	27	31		19	30	40	77
As	10	24	60		33	75	59		23	6	53	363
Bi	1.0	0.2	1.9		1.1	1.0	1.8		1.3	15.9	1.6	3.8
Sc	4	5	3		9	6	5		4	2	2	3
Tl	7.5	10.3	5.1		6.4	4.4	5.4		5.1	4.5	3.8	2.2
K/Rb	31	19	38		30	31	34		58	94	78	80
Zr/Hf	15	12	23		11	14	14		16	16	21	16
Nb/Ta	2.3	3.1	5.0		6.7	1.4	4.6		4.6	1.7	2.9	2.9

Rem.: major elements in wt.%, trace elements in ppm, elemental ratios by weight.